175

Fully developed turbulent pipe flow: a comparison between direct numerical simulation and experiment

By J. G. M. EGGELS,[1] F. UNGER,[2] M. H. WEISS,[3]
J. WESTERWEEL,[1] R. J. ADRIAN,[4] R. FRIEDRICH[2]
AND F. T. M. NIEUWSTADT[1]

[1] Delft University of Technology, Laboratory for Aero- and Hydrodynamics,
Rotterdamseweg 145, 2628 AL Delft, The Netherlands

[2] Lehrstuhl für Fluidmechanik, Technische Universität München, Arcisstrasse 21,
8000 München 2, Germany

[3] Novacor Research & Technology Corporation, 2928 – 16th Street NE, Calgary,
Alberta T2E 7K7, Canada

[4] University of Illinois at Urbana-Champaign, Department of Theoretical and Applied Mechanics,
104 South Wright Street, Urbana, IL 61801, USA

Direct numerical simulations (DNS) and experiments are carried out to study fully developed turbulent pipe flow at Reynolds number $Re_c \approx 7000$ based on centreline velocity and pipe diameter. The agreement between numerical and experimental results is excellent for the lower-order statistics (mean flow and turbulence intensities) and reasonably good for the higher-order statistics (skewness and flatness factors). To investigate the differences between fully developed turbulent flow in an axisymmetric pipe and a plane channel geometry, the present DNS results are compared to those obtained from a channel flow simulation. Beside the mean flow properties and turbulence statistics up to fourth order, the energy budgets of the Reynolds-stress components are computed and compared. The present results show that the mean velocity profile in the pipe fails to conform to the accepted law of the wall, in contrast to the channel flow. This confirms earlier observations reported in the literature. The statistics on fluctuating velocities, including the energy budgets of the Reynolds stresses, appear to be less affected by the axisymmetric pipe geometry. Only the skewness factor of the normal-to-the-wall velocity fluctuations differs in the pipe flow compared to the channel flow. The energy budgets illustrate that the normal-to-the-wall velocity fluctuations in the pipe are altered owing to a different 'impingement' or 'splatting' mechanism close to the curved wall.

1. Introduction

Direct numerical simulation (DNS) is an established numerical technique to study the details of turbulent flows. Databases generated by DNS provide results on turbulent flow statistics which are in good agreement with experiments (e.g. Kim, Moin & Moser 1987; Spalart 1988; Antonia *et al.* 1992). These databases also offer the opportunity to extract information from the flow field which cannot, or only with much difficulty, be obtained from experiments. The availability of this detailed flow information has certainly improved our understanding of physical processes in

turbulent flows which thus emphasizes the importance of DNS in present scientific research.

In 1987, Kim, Moin & Moser (hereinafter referred to as KMM) applied DNS to investigate fully developed turbulent flow between two parallel plates. Using nearly 4×10^6 gridpoints, they computed various statistics of the flow field at a Reynolds number based on mean centreline velocity and channel half-width h equal to 3300 ($h^+ = 180$). The general characteristics of the turbulence statistics showed good agreement with the experimental results of Eckelmann (1974) and Kreplin & Eckelmann (1979), except for some flow quantities in the wall layer. Recently, using the same code, a similar DNS was performed at a larger Reynolds number of 7900 ($h^+ = 390$). Together with the results of the previous DNS of KMM, Antonia *et al.* (1992) focused on low-Reynolds number effects in the inner region of the turbulent flow. The DNS and experimental results reported in their paper agreed well and indeed showed significant low-Reynolds-number effects. Beside these two computations, several other direct simulations of wall-bounded turbulent flows have been reported in the literature recently, e.g. plane channel flow by Lyons, Hanratty & McLaughlin (1991), developing turbulent boundary layer on a flat plate by Spalart (1988), turbulent flow in a rotating channel by Kristoffersen & Andersson (1993) and turbulent flow through a square duct by Gavrilakis (1992). These computations all have in common that they consider turbulent flow in a geometry with a rectangular cross-section or over a flat plate.

From experiments it is known that flows in geometries with a cylindrical cross-section show effects different from those observed in geometries with a rectangular cross-section. A well-known example is the difference in the rate of spreading of a plane and a round jet. Experimental data indicate that a round jet spreads approximately 15% less rapidly than a plane jet, which up to now is largely unexplained. Also for plane channel and axisymmetric pipe flows, experimental data show remarkable differences which are due to the different flow geometry. Patel & Head (1969) already reported observed deviations in mean velocity profiles obtained from fully developed turbulent channel and pipe flow measurements. They demonstrated that the flow in a pipe fails to conform to the accepted law of the wall even at Reynolds numbers considerably above 3000. In contrast, turbulent channel flows appear already to match the law of the wall at these low Reynolds numbers. Patel & Head concluded that 'at least some of the differences between pipe and channel flow results may be explained by the differences between axisymmetric and plane flow'.

Later, Huffman & Bradshaw (1972) analysing existing experimental data also showed differences in the logarithmic form of the velocity distribution obtained from pipe and channel flow measurements. They concluded that von Kármán's constant κ in low-Reynolds-number turbulent flows appears to be fixed at a best-fit value of 0.41, but that the additive constant C depends on external influences, e.g. transverse curvature effects. The dependence of C on transverse curvature would illustrate that the viscous sublayer is more sensitive to the transverse curvature than the rest of the inner layer. For increasing Reynolds numbers ($Re_\tau = u_\tau D/\nu > 2000$), the constant C also tends to become constant at a value close to 5.0 (Huffman & Bradshaw 1972).

In flows where a logarithmic velocity distribution is established, its extent appears to be different in an axisymmetric geometry compared to a plane geometry. Although no proof of existence of a logarithmic law is valid for distances from the surface more than, say, 0.1–0.2 times the half-width of the flow, the experimental results of Wei & Willmarth (1989) obtained from turbulent channel flow measurements, show a mean streamwise velocity profile following the logarithmic velocity distribution up to the

centreline of the channel ($y^+ > 1000$) for Re equal to 40×10^3. Laufer (1954) and Lawn (1971), in experiments on turbulent pipe flow at nearly the same Reynolds number, obtained mean velocity profiles matching the logarithmic distribution only up to $y^+ = 300$. Beyond $y^+ = 300$, the mean velocities exceeded the logarithmic distribution, indicating the presence of a wake region near the centreline of the pipe.

Considering these experimental observations, it becomes clear that an axisymmetric geometry affects the appearance of a logarithmic velocity distribution with respect to (i) the (lowest) Reynolds number at which a logarithmic velocity distribution is obtained, (ii) the values of κ and C in the logarithmic distribution and (iii) the apparent radial extent of this distribution.

Until now, comparisons of statistics between pipe and channel flows appear to be restricted to mean velocity profiles for which some differences are already observed. To investigate whether the axisymmetric flow geometry also affects the statistics of the fluctuating velocities, detailed statistical results of DNS on low-Reynolds-number turbulent pipe flow are reported in this paper. First, the results of two DNS computations are compared to corresponding experimental results to verify the numerical data. These experimental results are obtained using three different measurement techniques in two different experimental facilities. Next, the DNS results are compared to the data of KMM obtained from their DNS of fully developed turbulent channel flow at exactly the same Reynolds number (Re_τ based on wall friction velocity u_τ and channel half-width h or pipe radius R in both cases equals 180). The similarities and differences between axisymmetric and plane flow are elucidated for various flow statistics, including higher-order moments and energy budgets of the Reynolds stresses. Where possible, the observed differences are explained in terms of a different flow geometry.

The DNS computations were performed independently by Eggels & Nieuwstadt and by Unger & Friedrich, both using a similar code, the numerical procedures of which are discussed briefly in the next section. The hot-wire anemometry (HWA) measurements were carried out by Weiss (see Weiss 1993); the laser Doppler anemometry (LDA) and particle image velocimetry (PIV) measurements were performed by Westerweel & Adrian (see Westerweel 1993). The experimental methods and apparatus are described in §3. The statistical results of the simulations and experiments are compared in §4. From the DNS data, the energy balances of the Reynolds-stress components are computed and shown in §5. Finally, a summary and the conclusions of the present study are reported in §6.

2. Numerical procedures for the DNS computations

2.1. *Computational domain and numerical resolution*

The turbulent pipe flow is studied in the cylindrical geometry shown in figure 1 (a). The diameter of the pipe is denoted by D, and the length of the computational domain by L, with $L = 5D$. The Reynolds number, based on pipe diameter D and on centreline velocity U_c equals approximately 7000 (based on mean velocity U_b and shear stress velocity u_τ, it is 5300 and 360 respectively). Periodic boundary conditions for velocity components and pressure are applied in the circumferential direction. At the pipe wall no-slip boundary conditions are imposed for all velocity components whereas Neumann boundary conditions are used for the pressure. Since the fully developed turbulent pipe flow considered here is homogeneous in the streamwise direction, periodic boundary conditions are also imposed in the axial direction. However, the length of the computational domain must be chosen long enough to include even the

(*a*)

(*b*)

(*c*)

(*d*)
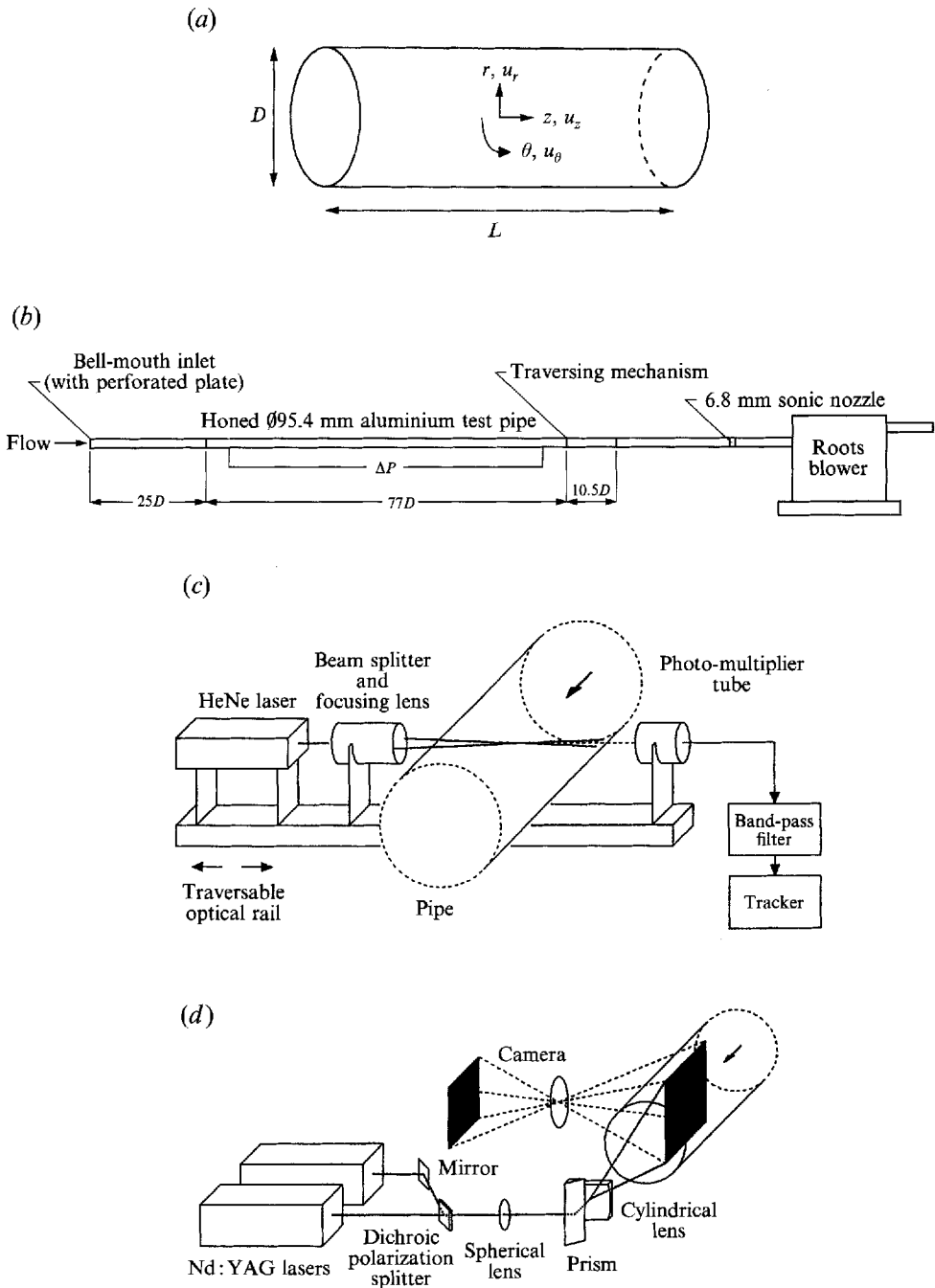
FIGURE 1. (*a*) Flow geometry and coordinate system used for turbulent pipe flow simulations. (*b*) Experimental apparatus for single hot-wire anemometer measurements (*c*) Optical configuration for the LDA measurements. (*d*) Optical configuration for the PIV measurements.

largest-scale structures. This can be achieved by ensuring that the fluctuating velocities are uncorrelated at a streamwise separation of half the lengthscale *L*. We will return to this point in §4.2 when the results are presented.

To justify a direct numerical simulation without inclusion of any turbulence model,

the spatial and temporal resolution must be high enough to capture even the smallest scales of the turbulent motion. Grötzbach (1983) formulated several criteria which are followed here to estimate the numerical resolution required. His criterion (i) concerns the size of the computational domain which should be sufficiently large to record all relevant large-scale structures. This will be discussed in §4.2. Criteria (ii) and (iii) require that the normal-to-the-wall grid width distribution must be able to resolve the steep gradients in the velocity field near the wall and that the mean grid width must be smaller than the smallest relevant turbulence elements. According to Grötzbach, quantification of these qualitative criteria can be a serious problem, but the latter two can be met by taking at least three gridpoints within the viscous sublayer and by ensuring that the mean grid width Δ satisfies $\Delta \leqslant \pi \eta$, with η the Kolmogorov lengthscale. The latter criterion also applies for the imposed time-step Δt which must satisfy $\Delta t \leqslant \tau$, with τ the Kolmogorov timescale.

The present computations are carried out with $96 \times 128 \times 256$ gridpoints equally spaced in the r, θ, z-direction respectively. The gridspacing is computed as $\Delta r^+ \approx 1.88$ and $\Delta z^+ \approx 7.03$ in terms of viscous wall units (ν / u_τ). The circumferential gridspacing varies linearly with r and reaches a minimum value $(\frac{1}{2} \Delta r \Delta \theta)^+ \approx 0.05$ near the centreline of the pipe and a maximum value $(\frac{1}{2} D \Delta \theta)^+ \approx 8.84$ at the pipe wall. The first gridpoint near the pipe wall at which the axial velocity is computed is located at $y^+ = 0.94$. With $\Delta r^+ \approx 1.88$, it follows that three gridpoints are placed within the viscous sublayer, the depth of which approximately equals 5 wall units. Hence, criterion (ii) is satisfied. The mean grid width Δ computed as $\Delta^+ = [(r \Delta r \Delta \theta \Delta z)^{\frac{1}{3}}]^+$ equals 4.9 wall units near the wall where Δ^+ is largest. The averaged Kolmogorov lengthscale η^+ in wall units and based on the volume-averaged viscous dissipation $\langle \epsilon \rangle$, is estimated from an equilibrium state between the energy production by the mean pressure gradient and the viscous energy dissipation. For the given Reynolds number, η^+ equals approximately 1.6 (KMM obtained $\eta^+ \approx 2$ for their turbulent channel flow, and Antonia *et al.* (1992) 1.5 to 42 wall units without any dependence on Reynolds number). Thus $\pi \eta^+$ equals approximately 5.0 and hence criterion (iii) is also satisfied. The present gridspacing resembles the gridspacing employed by KMM who used a mean gridspacing of 2.8, 7 and 12 viscous wall units in the normal-to-the-wall, spanwise and streamwise directions respectively. However, they employ a non-uniform grid in the normal-to-the-wall direction which allows them to locate more gridpoints in the sublayer (first gridpoint at $y^+ \approx 0.05$). With the aid of this non-uniform grid, spatial variations in the normal-to-the-wall direction can be represented more accurately because of the larger number of gridpoints. It does not naturally imply that the spatial resolution in the near-wall region is much better. To achieve such a better resolution, a finer gridspacing in streamwise and circumferential (spanwise) directions would be more effective in our opinion. In these directions, the spatial resolution in the present DNS computations is very similar to that employed by KMM.

The time-step Δt in the numerical simulations equals $0.0002 t^*$, where t^* is the dimensionless timescale defined as the ratio of pipe diameter D and friction velocity u_τ. Similar to the procedure above where the Kolmogorov lengthscale was expressed in terms of wall units, the Kolmogorov timescale τ can be expressed in terms of t^*. We then obtain $\tau = 0.0068 t^*$. Clearly, the imposed time-step Δt is much smaller than the Kolmogorov timescale, indicating that the resolution in time is also sufficiently fine to resolve all scales of motion. On physical grounds, Δt could have been increased, but the admissible time-step is restricted to avoid numerical instabilities (Schumann 1975). This is a major disadvantage of the explicit time-integration schemes employed, which will be discussed in the following subsection.

2.2. *Numerical techniques*

The spatial and temporal evolution of an incompressible Newtonian fluid flow can be written in dimensionless form, using u_τ and D as velocity and length scales for normalization, as

$$\nabla \cdot v = 0, \tag{1}$$

$$\frac{\partial v}{\partial t} + (v \cdot \nabla)v = -\nabla p + \frac{1}{Re_\tau}\nabla^2 v \tag{2}$$

with v the velocity vector. Re_τ is thus defined as $u_\tau D/\nu$. The pressure gradient $-\nabla p$ is split into a mean pressure gradient $-\nabla P$ and a fluctuating pressure gradient $-\nabla p'$ such that periodic boundary conditions in the streamwise direction can be employed for the fluctuating pressure p'. The mean pressure gradient $-\nabla P$ only has a non-zero component in the streamwise direction in order to balance the net viscous friction at the pipe wall. This non-zero component equals $4u_\tau^2/D$ in dimensional form, i.e. it equals 4 when scaled with D and u_τ.

Equations (1) and (2) are discretized by means of the finite volume technique according to which they are integrated over a small gridvolume (Schumann 1973). A staggered grid is used in which the pressure is defined at the centre of each gridvolume and the velocity components at the interfaces of the gridvolumes. To carry out the integration numerically, the midpoint integration rule is used. Velocity components and their derivatives, which have to be determined at locations in between their corresponding positions in the gridvolume, are obtained by linear interpolation and central differences respectively. As a result, the spatial discretization is of second-order accuracy. The basic numerical technique used here thus differs significantly from the one used by KMM and Antonia *et al.* (1992) who employed a spectral method to represent the spatial derivatives. At a similar numerical resolution, spectral methods provide better estimates for the spatial derivatives, especially at high wavenumbers (small scales) where finite difference methods may suffer from numerical dispersion and diffusion. On the other hand, spectral methods are only applicable for flow computations in simple geometries with periodic boundary conditions in one or more directions.

In a comparative study, Rai & Moin (1989) examined the influence of a finite difference *vs.* a spectral approach on the statistical results by comparing the turbulence statistics of the KMM computations with those obtained using various finite difference techniques. They concluded that the prevalent method for DNS of turbulent flows is the spectral method, but that for complex geometries finite difference techniques, especially high-order accurate upwind-biased methods, are good candidates. Their statistical results obtained from the finite difference computations showed a reasonable, but not excellent, agreement with the results obtained earlier with the spectral method. However, the numerical resolution in these finite difference computations ($64 \times 65 \times 64$ and $128 \times 85 \times 128$ gridpoints *vs.* $192 \times 129 \times 160$ gridpoints in case of the spectral method) is most likely to be insufficient to justify a conclusion on the performance of finite difference schemes. With this coarse numerical resolution, not all relevant scales of turbulent motion are captured. In §§4 and 5 of the present work, it will be shown that a DNS computation based on the finite volume technique generates realistic statistical results provided that the numerical resolution is sufficiently fine. A similar conclusion can be drawn from the DNS results on turbulent duct flow reported by Gavrilakis (1992) and on the rotating channel flow by Kristoffersen & Andersson (1993).

In view of the cylindrical flow geometry considered in our work, the present computations are performed using a cylindrical coordinate system in equations (1) and (2). We will now briefly consider some difficulties caused by the application of this cylindrical coordinate system. Owing to the curvature of the coordinate system, the governing equations contain a singularity at the centreline of the pipe ($r = 0$). Using the finite volume technique, this singularity can be circumvented rather easily without much special effort.† Beside the singularity at the centreline, the curvature of the cylindrical coordinate system also affects the time-integration. The admissible time-step in explicit time-integration schemes, which are mostly used for these time-dependent numerical simulations, is restricted by stability criteria to avoid numerical instabilities (Schumann 1973, 1975). For the advective terms, the allowable time-step is linearly proportional to the gridspacing; for the diffusive terms, to the square of the gridspacing. Since the gridspacing in the circumferential direction is proportional to $r\Delta\theta$ (*vs.* constant Δr and Δz in the radial and axial directions respectively), the admissible time-step is severely limited by the small gridspacing close to the centreline where r becomes of order Δr. To avoid a too strong restriction on the time-step, all terms containing derivatives in the circumferential direction are treated implicitly in time: the advective terms with the Crank–Nicolson scheme and the diffusive terms with the Euler-backward scheme (Unger & Friedrich also used the Euler-backward scheme for the advective terms). All other terms involving derivatives in the radial and axial directions remain treated explicitly in time: the advective terms with the leap-frog scheme and the diffusive terms with the lagged Euler-forward scheme. The fluctuating pressure distribution p' is obtained from a predictor–corrector technique which results in a Poisson equation for p'. A FFT-based routine is used to solve this Poisson equation at every time-step. For a more extended description of the numerical details of the codes, we refer to Unger & Friedrich (1993) and Eggels (1994).

The DNS computations are initiated from randomly generated fields with mean and r.m.s. velocities fitted to preliminary HWA data. Since the fluctuations in these random velocity fields are large on small spatial scales, the viscous dissipation is large which appears to remove the initial velocity fluctuations very effectively and to laminarize the flow. To circumvent such a decay of fluctuations, the viscosity was reduced initially. A simulation using the same numerical resolution but with an artificially reduced viscosity ($Re_\tau \approx 6000$) was performed first by Eggels & Nieuwstadt. At $t = 1.0t^*$, with t^* the dimensionless timescale D/u_τ, the resulting flow field was used as the initial field for the actual DNS at the correct Reynolds number ($Re_\tau = 360$). Unger & Friedrich followed a somewhat different approach. They started with $Re_\tau = 3000$ at $t = 0$ and gradually reduced Re_τ to end up with $Re_\tau = 500$ at $t = 1.0t^*$. This flow field was then used to start the actual DNS at $Re_\tau = 360$. The time advancement in the DNS by Eggels & Nieuwstadt was carried out until $t = 10t^*$ to achieve a flow field independent of the random initial conditions (Unger & Friedrich advanced until $t = 12t^*$). At $t = 10t^*$ (respectively $t = 12t^*$), the total shear stress profiles versus r/D showed an almost linear distribution, indicating that the computations had reached a nearly statistically steady state. The averaged deviation of the total shear stress profile with respect to the linear distribution is less than $0.036\rho u_\tau^2$ (the maximum deviation is less than $0.07\rho u_\tau^2$). From $t = 10t^*$ and $t = 12t^*$, the computations were continued until $t = 14t^*$ and $t = 16t^*$ respectively. In these intervals, the final statistical data have been accumulated by spatial averaging in the homogeneous streamwise and circumferential directions and

---

† The radial discretization near the centreline is not treated exactly similarly in the two codes. For details, we refer to Unger & Friedrich (1993) and Eggels (1994).

by time averaging over 41 (nearly independent) data fields, all separated by $0.1t^*$. The DNS performed by Eggels & Nieuwstadt (referred to as DNS(E)) was carried out on the Cray Y-MP4/464 computer of the Academic Computing Services Center (SARA) in Amsterdam and required 39.6 Mwords of memory. The total CPU-time was approximately 160 hours, or about 11.4 CPU-hours per t^*. Each complete time-step took about 8.2 CPU-seconds for the given numerical resolution of $96 \times 128 \times 256$ gridpoints. The DNS by Unger & Friedrich (referred to as DNS(U)), was carried out on the Cray Y-MP4/464 computer of the Leibniz computer centre (LRZ) of the Bavarian Academy of Sciences in Munich. The computer requirements corresponding to their DNS are respectively: 29.7 Mwords memory, total CPU-time of 152 hours, 9.5 CPU-hours per t^* and 6.8 CPU-seconds per time-step. Their code is less memory consuming than the code used by Eggels & Nieuwstadt because of a different internal storage of the three-dimensional velocity and pressure fields.

3. Experimental methods and apparatus

3.1. *HWA measurements*

A single-wire anemometer probe traversed the pipe cross-section 101 diameters downstream from the inlet to obtain profiles of mean and fluctuating velocity in a fully developed turbulent pipe flow. The measurements were carried out in the experimental set-up shown in figure 1(*b*). Quiescent air from the laboratory was drawn through a test section of straight, honed aluminium pipe by a Roots blower via a calibrated sonic nozzle situated between the test section and the blower. Use of a choked sonic nozzle allowed precise measurement of the mass flow rate ($< 0.5\%$ absolute error) while also isolating the test section from pressure fluctuations induced by the blower.

The test section consisted of a bell-mouth inlet followed by three pieces of aluminium pipe, identically honed to an internal diameter of 95.4 mm with a surface roughness of less than 0.5 μm. Concentric alignment of better than 50 μm (< 0.2 wall units for $Re_b = 5450$) between the various pieces of test piping was accomplished through special split-ring flange joints with o-ring seals. A disc, perforated with 4.5 mm diameter holes on 6.5 mm centres (porosity $= 44\%$), was located at the inlet plane of the bell-mouth to act as a flow tripping device for the 2.375 m ($= 25D$) flow development section, followed by a 7.316 m ($= 77D$) test pipe and an additional 1.000 m ($= 10.5D$) pipe. The hot-wire sensor traversing mechanism is located 9.691 m ($= 101.5D$) downstream of the inlet in between the second and third honed aluminium pipe sections. The traversing mechanism consists of a 10 mm wide annular ring, of the same internal diameter as the aluminium pipe, on which a micrometer-driven slide mechanism is mounted to accurately locate (± 0.01 mm) and vary the radial position of the hot-wire probe. In addition, the ring can be rotated in a plane perpendicular to the pipe axis in order to vary the azimuthal position of the probe. Following the total test section of $112.5D$ aluminium pipe is a measurement section consisting of $25D$ of 101 mm diameter plastic pipe and a 6.8 mm diameter calibrated sonic nozzle to measure the mass flow rate. Additional plastic pipe connects the nozzle to the Roots blower piping.

The single wire is first calibrated with a laminar pipe flow calibration system which develops velocities in the range of 0.05–1.5 m s^{-1}. The probe axis is aligned with the centreline of the pipe and the flow varied to obtain temperature-compensated calibration curves of anemometer bridge voltage *vs.* velocity. The probe is then mounted in the traversing mechanism using a 90° probe holder which locates the probe tip 95 mm upstream of the traversing ring in undisturbed flow to measure the velocity profiles. The signal from the TSI IFA 100 constant-temperature anemometer circuit is

sampled every 1 ms (well below the smallest timescale expected: $\tau' = \nu/u_\tau^2 \approx 5$ ms and Kolmogorov timescale $\tau \approx 12$ ms) using an electronic data acquisition system and analysed with a personal computer.

The 4 μm diameter platinum-coated tungsten single-wire probe sensor has a length of 1 mm (approximately 4.0 wall units) and was used to measure the instantaneous axial velocity component. The accuracy of the mean velocity measurement ranges from 1% at the pipe centreline to about 4% very close to the wall. Reproducible measurements of mean and fluctuating velocity as well as higher-order turbulence statistics were obtained with this technique. A precision micro-manometer is used to measure the pressure drop along the test section from which the friction velocity is determined with an accuracy of 1.5%. Further details concerning the HWA measurements can be found in Weiss (1993).

3.2. *LDA and PIV measurements*

The laser Doppler anemometry and particle image velocimetry measurements were made near the end of a 17 m ($= 134D$) smooth pipe with an inner diameter of 127 mm and a Reynolds number of 5450 based on the mean velocity and the diameter of the pipe.† The pipe flow facility was previously used for accurate hot-wire measurements of fully developed turbulent flow at a Reynolds number of 50000 (Lekakis 1988). The air flow through the pipe was driven by a blower, powered by a d.c. motor with a variable transmission. The air passed a settling chamber, a honeycomb, and a square grid with a mesh size of 1 mm and a solidity of about 1, before it entered the pipe. The grid introduced an initial disturbance, which reduced the inlet length that was required before the flow became fully turbulent. At high Reynolds numbers an inlet length of 40 to 50 pipe diameters is considered sufficiently long (Schlichting 1979) to produce a fully developed turbulent flow. At low Reynolds numbers, the development of the flow also depends on the flow conditions at the pipe inlet: to obtain a fully developed turbulent pipe flow, the turbulence level at the pipe inlet (i.e. directly behind the grid) should be sufficiently high (Wygnanski & Champagne 1973). Measurements carried out with LDA indicated that the flow at the test section for the PIV measurements was fully developed. This indirectly verified that the initial disturbances caused by the grid at the pipe inlet were sufficient to obtain fully developed turbulent flow.

Using LDA, the axial component of the velocity was measured with a 5 mW HeNe laser in a dual-beam configuration, with a photo-multiplier in the forward scattering direction (see figure 1c). The laser beam was split into two parallel beams with a separation of 48 mm, and these two beams were focused on a measurement spot with a 250 mm focal length lens. The measurement volume defined by the e^{-2} optical intensity was 250 μm in diameter and 2.6 mm long (in terms of viscous wall units respectively 0.7 and 7.6 units). The output signal from a TSI 1090 frequency tracker was sampled at 10 Hz (0.1 s roughly corresponds to an Eulerian timescale, estimated by dividing the pipe diameter by centreline velocity) and integrated over 300 s to determine the mean value of the velocity. The root-mean-square (r.m.s.) fluctuating velocity was measured with a digital r.m.s. voltmeter and an integration time constant of 100 s. The estimated statistical sampling errors for the measured velocities were about 0.3% for the mean and 1–2% for the r.m.s.

For both LDA and PIV measurements, the flow was seeded with 1–2 μm diameter

---

† The mean velocity and Reynolds number based on this mean velocity slightly differ here from the values reported in the original paper by Westerweel *et al.* (1993) because the mean velocity profile has been integrated numerically using Simpson's integration rule instead of the trapezium rule adopted originally.

oil droplets generated by two atomizers. The droplets were small enough to follow the motions of the air flow very accurately. The PIV laser sheet illuminated a plane through the centreline of the pipe, and a view area that included the full diameter of the pipe was photographed. The optical system for the PIV measurements is sketched in figure 1(*d*). Light pulses were provided by two frequency-doubled Nd:YAG pulsed lasers with an energy of 130 mJ per pulse at a repetition rate of 20 Hz. The firing of the lasers was accurately synchronized with a time delay of 0.3 ms (accuracy to ± one part in 10^5). The orthogonally polarized laser beams were combined into a double-pulsed beam by a polarization splitter plate. A prism at the pipe outlet reflected the beam 90° into the pipe. A spherical lens (1000 mm focal length) combined with a cylindrical lens (−100 mm focal length) transformed the beam into a thin, vertical light sheet that spanned the entire diameter of the pipe with a thickness of 0.4 mm (= 1.15 viscous wall units). The light sheet had a non-uniform light distribution, with a maximum intensity near the centreline and with gradually reducing intensity towards the pipe wall. In total 33 photographs were taken which all covered the entire pipe diameter D and a length of 1.11D in the streamwise direction. Each photograph yielded instantaneous two-dimensional data sets of the axial and radial velocities at 8500 points. The PIV recordings were analysed with the interrogation system described by Landreth & Adrian (1990). For specific details of the latter analysis and an extended description of the experimental set-up, refer to Westerweel (1993) (some details are also reported by Westerweel *et al.* 1993).

4. Turbulence statistics

4.1. *Mean flow properties*

Several mean flow properties obtained from simulations and measurements are listed in table 1. The results reported by KMM for their channel flow are given for comparison in the last column. Several quantities listed in this table are defined as follows. U_b is the mean (or bulk) velocity given by

$$U_b \pi R^2 = 2\pi \int_0^R r u_z(r)\,\mathrm{d}r. \tag{3}$$

Some characteristics of the mean velocity profile are expressed by the following lengthscales: the displacement thickness δ^*, which is defined as

$$\delta^*(2R - \delta^*) = 2\int_0^R r\left(1 - \frac{u_z(r)}{U_c}\right)\mathrm{d}r, \tag{4}$$

and the momentum thickness θ^* which is defined similarly to δ^*:

$$\theta^*(2R - \theta^*) = 2\int_0^R r\frac{u_z(r)}{U_c}\left(1 - \frac{u_z(r)}{U_c}\right)\mathrm{d}r, \tag{5}$$

with U_c the centreline velocity. These two formulae are somewhat different from their usual definitions because of the cylindrical coordinate system (Eggels 1994).

The numerical and experimental pipe flow results in table 1 agree to within a few percent. Blasius' law $C_f = 0.079\,Re^{-0.25}$ (*Re* must be based on pipe diameter and mean velocity) is used to determine the skin friction coefficient of turbulent pipe flow. The values of $C_f = \tau_w/\frac{1}{2}\rho U_b^2$ computed from the DNS data equal 9.22×10^{-3} and 9.21×10^{-3} respectively which is indeed in excellent agreement with Blasius' value of
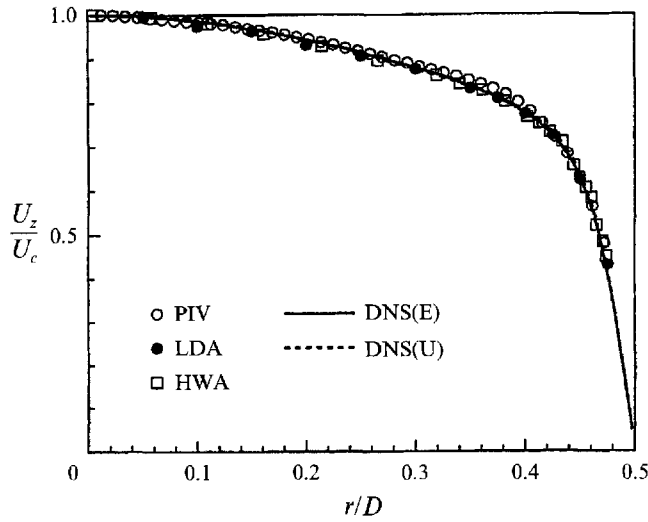
FIGURE 2. Axial mean velocity normalized by the centreline velocity U_c as function of the distance from the centreline.

	DNS(E)	DNS(U)	PIV	LDA	HWA	KMM
$Re_c = U_c D/\nu$	6950	6950	7100	7200	7350	6600
$Re_b = U_b D/\nu$	5300	5300	5450	5450	5600	5600
$Re_\tau = u_\tau D/\nu$	360	360	366	371	379	360
U_c/u_τ	19.31	19.29	19.38	19.39	19.40	18.20
U_b/u_τ	14.73	14.74	14.88	14.68	14.76	15.63
U_c/U_b	1.31	1.31	1.30	1.32	1.31	1.16
$C_f = \tau_w/\frac{1}{2}\rho U_b^2$	9.22×10^{-3}	9.21×10^{-3}	9.03×10^{-3}	9.28×10^{-3}	9.18×10^{-3}	8.18×10^{-3}
δ^*/R	0.127	0.126	0.124	0.130	0.128	0.141
θ^*/R	0.068	0.068	0.068	0.071	0.070	0.087
$H = \delta^*/\theta^*$	1.86	1.85	1.83	1.83	1.82	1.62
G	8.91	8.85	8.78	8.79	8.73	6.97

TABLE 1. Mean flow properties obtained from numerical simulations and experiments. The results obtained by Kim *et al.* (1987) for turbulent channel flow are shown in the last column (KMM). The various parameters are defined as follows: U_c is the centreline velocity, U_b the mean velocity, u_τ the wall shear stress velocity, D the pipe diameter or full channel width, ν the kinematic viscosity, C_f the friction coefficient, τ_w the wall shear stress equal to ρu_τ^2, δ^* and θ^* the displacement and momentum thicknesses, R the pipe radius or channel half-width and H the shape factor. The parameter G in the last row is defined as $G = U_c/u_\tau((H-1)/H)$.

9.26×10^{-3} for $Re = 5300$. From table 1, it follows that the mean flow properties obtained from axisymmetric pipe flow and plane channel flow clearly differ. In particular, the ratio U_b/u_τ is larger in channel flow than in pipe flow which causes C_f to be smaller. Furthermore, the ratio U_c/U_b obtained from the pipe flow results exceeds the corresponding value in the channel flow. It is interesting to note that the present pipe flow results agree extremely well with the recent DNS results of turbulent flow in a square duct by Gavrilakis (1992). Despite the fact that the square duct flow shows a secondary flow pattern (hence, the flow is homogeneous in the streamwise direction only), the overall mean flow properties are in very close agreement with the present results (Gavrilakis reports $U_c/U_b = 1.33$, $U_b/u_\tau = 14.7$ and $C_f = 9.26 \times 10^{-3}$).

J. G. M. Eggels and others
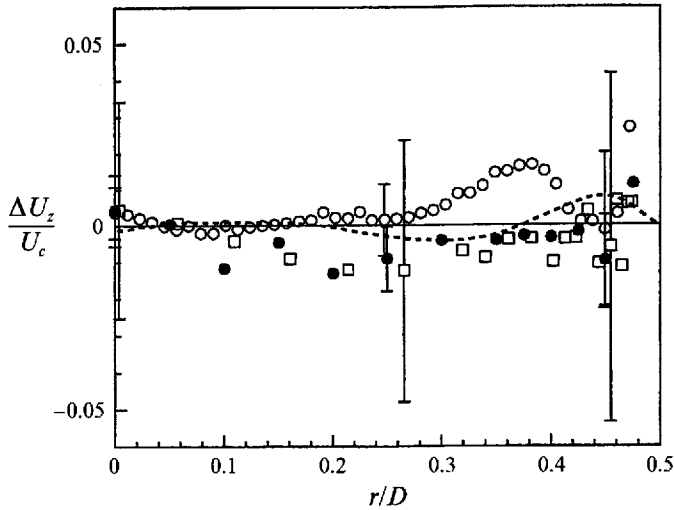
FIGURE 3. Residual mean velocity normalized by the centreline velocity U_c as function of the distance from the centreline. These residuals are computed with respect to the DNS(E) data. The error bars shown for the measurements indicate the 95% reliability intervals computed from the experimental data. For symbols see figure 2.

This illustrates that the additional wall friction at the 'side'-walls of the pipe and the square duct causes the mean flow properties to be different from those obtained for plane channel flow.

The mean velocity profile normalized by the centreline velocity is shown in figure 2. The numerical and experimental results coincide for all r/D. The DNS(U) profile is not visible here because it completely collapses onto the DNS(E) profile. To magnify the deviations between the numerical simulations and the experiments, the residual velocities with respect to the DNS(E) data are plotted in figure 3. These residual velocities are also normalized by the corresponding centreline velocity and show only small deviations ($|\Delta U_z/U_c| < 0.02$). For the experimental results, the 95% reliability intervals shown by the error bars are estimated at three radial positions ($r/D \approx 0$, 0.25 and 0.45). The numerical and experimental results do not differ significantly according to these 95% reliability intervals. The DNS results also show minor deviations in the near-wall region. These deviations could be attributed to the (shifted) sampling intervals with finite lengths of $4t^*$, with t^* defined as D/u_τ. We have plotted the bulk velocity and wall shear stress as function of time and observed low-frequency oscillations (not shown here). In particular, the bulk velocity U_b showed a nearly sinusoidal behaviour with a characteristic timescale approximately equal to $6t^*$ (amplitude of order $0.1u_\tau$). The sampling interval of $4t^*$ is rather short compared to this timescale. As a result, low-frequency oscillations appearing as the deviations observed in figure 3, are not completely removed from the mean velocity profiles.

The mean velocity sealed on inner variables is shown in figure 4(a, b). The viscous sublayer is well resolved in the numerical simulations, yielding the linear velocity distribution $u_z^+ = y^+$ for $y^+ < 5$. At larger distances from the wall ($y^+ > 30$), the logarithmic velocity distribution with 'universal' constants (von Kármán's constant $\kappa = 0.4$ and the additive constant $C = 5.5$, which is somewhat larger than the universal value 5.0 to compensate for low-Reynolds number effects; see KMM) is not followed either in the numerical simulations or the experiments, as shown in figure 4(a). In contrast, the DNS results of KMM exhibit a good agreement with the logarithmic
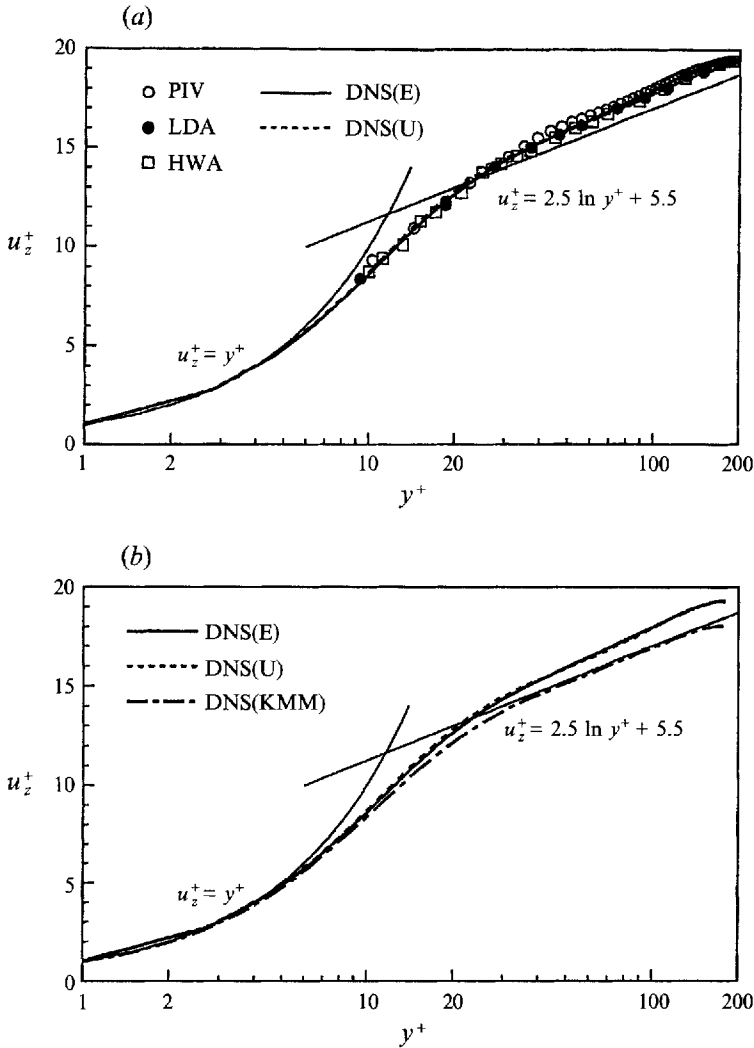
FIGURE 4. Axial mean velocity scaled on inner variables: (*a*) the present numerical and experimental data, (*b*) a comparison of the present DNS data to the DNS data obtained by KMM for their DNS of turbulent channel flow. The thin solid lines represent the universal velocity distributions.

velocity distribution for $y^+ > 30$. Figure 4(*b*) thus confirms the observations by Patel & Head (1969) who demonstrated that the flow in a pipe fails to conform to the accepted law of the wall even at Reynolds numbers considerably above 3000, in contrast to plane channel flow. Only for Reynolds numbers (much) larger than the present one does turbulent pipe flow exhibit a logarithmic velocity distribution, at least over a part of the cross-section (see e.g. Laufer 1954 and Lawn 1971). A best-fit of the logarithmic velocity distribution to the DNS(E) pipe flow data is given by $u_z^+ = 2.86 \ln y^+ + 4.8$ with the best-fit von Kármán constant $\kappa' = 0.35$ and additive constant $C' = 4.8$. This value of the von Kármán constant is estimated from figure 5 where a logarithmic velocity distribution should be identified with a constant value of the velocity gradient shown here (see also Spalart 1988). The value of C' is obtained by substituting the velocity at $y^+ \approx 60$ into the logarithmic distribution for the given value of the von Kármán constant. For the DNS(E) pipe flow data considered here, both κ

and C differ from the 'universal' values 0.4 and 5.5 respectively (from the KMM data, we obtain $\kappa = 0.40$ and $C = 5.4$ which is close to these values). The parameter plotted in figure 5 is sensitive to small variations of the velocity gradient, especially at large values of y^+. From figures 4(a) and 4(b), the deviations between the numerical simulations appeared to be small but once plotted in this way, the deviations are strongly magnified. From the DNS(U) data, we obtain $\kappa' = 0.38$ and $C' = 5.6$ if only the local minimum at $y^+ \approx 50$ in figure 5 is considered. These values differ from the DNS(E) results for which we obtained 0.35 and 4.8 respectively. On average ($40 < y^+ < 120$), however, the best-fit values of von Kármán's constant in both pipe flow simulations agree fairly well and clearly differ from the value found in plane channel flow.

At first glance, the present results appear to contradict the conclusions by Huffman & Bradshaw (1972) who obtained a quite constant value for κ, independent of transverse curvature effects. The latter effects are only accounted for in the constant C. However, one should ask whether the existence of a logarithmic velocity distribution is realistic for these low-Reynolds-number flows. Theoretically, the logarithmic velocity distribution is only justified at large Reynolds numbers in that part of the flow where $y^+ \geqslant 30$ and $y/D \leqslant 0.1$ hold simultaneously (Tennekes & Lumley 1972, chap. 5). The Reynolds number for which a logarithmic velocity distribution might be observed thus appears to be limited at the low end where $y^+ = 30$ and, at the same time, $y/D = 0.1$. This corresponds to $Re_\tau = 300$. In the present study $Re_\tau = 360$, which implies that at this low Reynolds number there is no firm theoretical base for the existence of a logarithmic velocity distribution with 'universal' constants. In view of these considerations, it remains somewhat surprising that the logarithmic velocity distribution is followed almost up to the centreline in the plane channel flow.

Admittedly, the present study would have been more complete if we had also performed DNS of plane channel flow using our finite volume approach and had confirmed the existence of the logarithmic velocity distribution in such a flow. Then, the deviations between the present DNS results and those of KMM could have been fully attributed to the different flow geometry rather than possibly being influenced by different numerics (see also §2.2). Unfortunately, we have not performed such a DNS. Nevertheless, in view of the following two arguments, the deviations between our DNS of pipe flow and the KMM channel flow data are most likely due to a different geometry rather than to different numerics: (a) the present DNS results are in excellent agreement with the various experimental data (see figures 3 and 4a), (b) Kristoffersen & Andersson (1993) *did* perform DNS of plane channel flow using a finite difference/finite volume approach and obtained excellent agreement with the logarithmic law of the wall, i.e. they showed that the same velocity distribution as found by KMM is obtained using the finite volume method.

4.2. *Two-point velocity correlations and spectra*

The two-point correlation coefficients of the fluctuating velocities obtained from the DNS(E) data are shown in figure 6(a–d) for various radial positions as functions of the streamwise separation z/D. To justify the adequacy of the length $L = 5D$ of the computational domain, the velocity fluctuations at a streamwise separation of half the pipe length should be uncorrelated. From figure 6(a–d), it appears that all two-point velocity correlation coefficients are negligibly small for $z/D = 2.5$ except for the streamwise velocity component near the wall (figures 6c and 6d). Here, the correlation coefficients remain rather large at approximately 0.08. Streamwise elongated flow structures are present in the near-wall region which cause the correlations to be non-
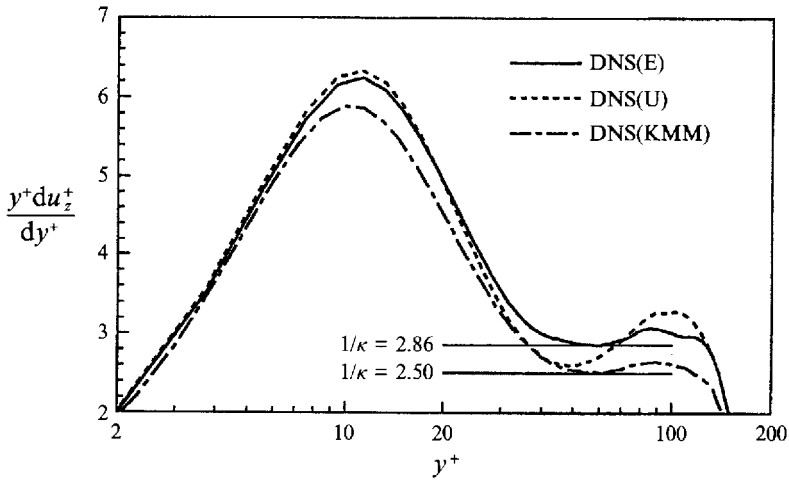
FIGURE 5. Dimensionless velocity gradient *vs.* the distance from the wall in wall units.

zero. These structures presumably consist of the so-called low-speed streaks which are very persistent and show long streamwise extents up to 1000 viscous wall units and transverse extents of typically 100 wall units. With the domain length L equal to 1800 wall units, it becomes clear that these low-speed streaks are a possible cause of the velocity correlations being non-zero. Although we have not yet investigated how the imposed domain length $L = 5D$ might affect other statistical results, we expect that the influence on the statistics will only be of minor importance. In the KMM channel flow simulation, the two-point correlation coefficients of the streamwise velocity fluctuations decay faster than in the pipe and reach zero at $x/\delta = 4$ or, in terms of the present variables, at $z/D = 2$.

The smooth variations that appear in the velocity correlations shown in figure 6(*a*) are caused by the data accumulation procedure used and should be considered as statistical errors. The correlation functions are computed using time averaging and spatial averaging in the homogeneous streamwise and circumferential directions, but close to the centreline the velocity fluctuations in the circumferential direction become strongly correlated because of small separation distances. As a result, spatial averaging in the circumferential direction does not contribute much to stable mean values. Near the centreline of the pipe, the statistics for u_r and u_θ are equal because of geometrical considerations.

One-dimensional wavenumber spectra of the fluctuating velocities are computed and shown in figure 7(*a–e*). The experimental and numerical spectra are normalized independently by the corresponding r.m.s. velocities and plotted at three radial positions ($r/D \approx 0$, $r/D \approx 0.25$ and $r/D \approx 0.45$) in figure 7(*a–c*). The PIV and DNS(E) results show good agreement within the wavenumber range from 5 to 50, except for the axial velocity fluctuations near the wall (figure 7*b*, solid line). This discrepancy is most likely related to the somewhat short domain length $L = 5D$ for which the correlation coefficient was already non-zero at $z/D = 2.5$ (figure 6*c*). At wavenumbers $k_z D > 50$, the PIV signal is obscured by noise, yielding a nearly constant energy level for all wavenumbers (see also Westerweel *et al.* 1993). In figure 7(*c*), the spectra for the axial velocity fluctuations are shown, obtained from DNS(E) and HWA. The agreement is similar as observed for the PIV data. The HWA data are also obscured by noise but at larger wavenumbers ($k_z D > 70$). The noise level in the HWA data is almost an order
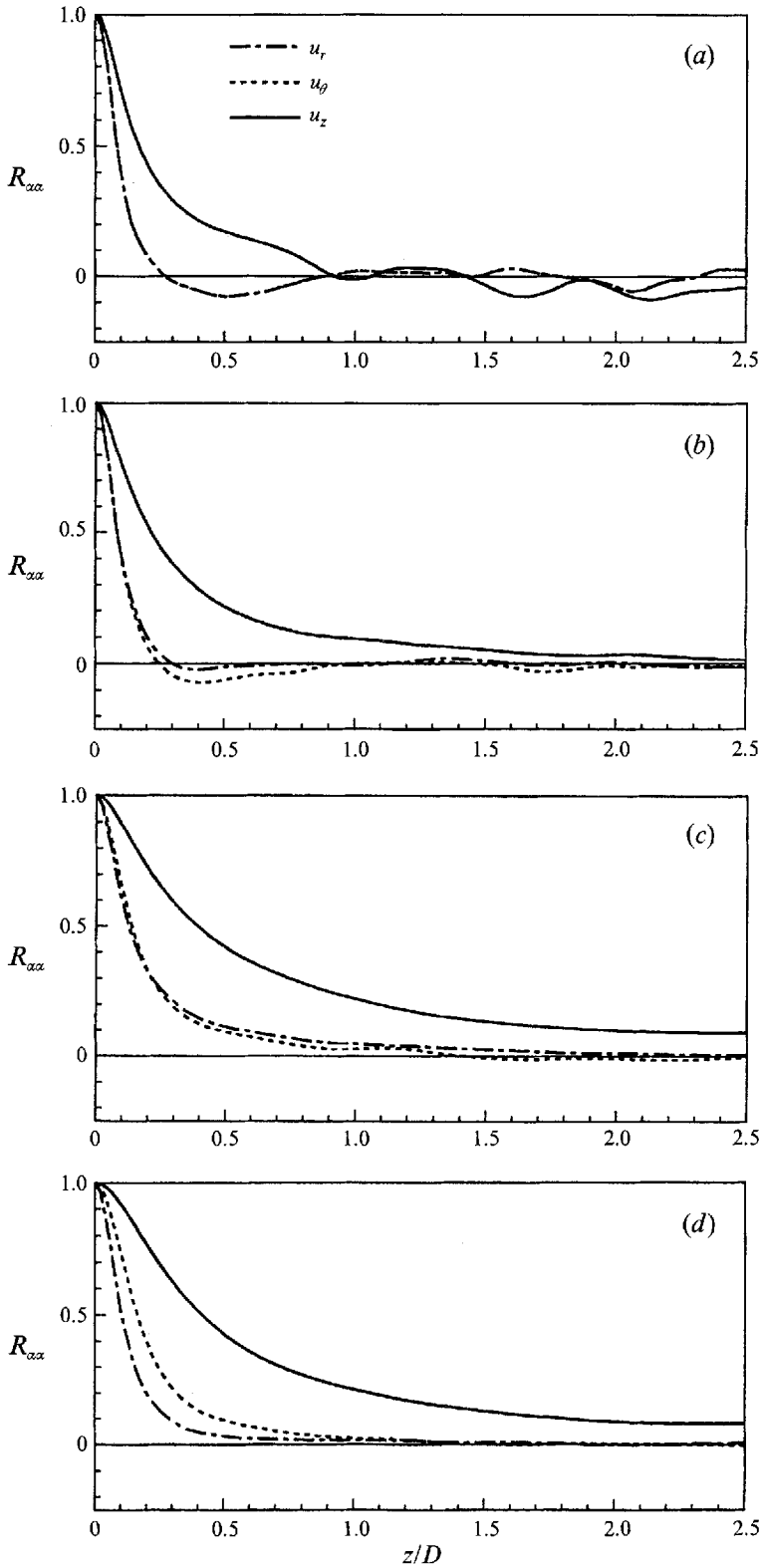
FIGURE 6(*a–d*). For caption see facing page.

of magnitude less than in the PIV data. The HWA spectra are obtained from time series whereas line series are used for the DNS(E) and PIV spectra. For the conversion of the time series into line series, the local mean velocity in the streamwise direction is used as the convection velocity. The close agreement between all spectra shows that Taylor's frozen field hypothesis is correct for the flow conditions considered here. In figures 7(d) and 7(e), the normalized spectra computed from the DNS(U) data are compared to the corresponding spectra obtained from the plane channel flow DNS by Gilbert & Kleiser (1991). As in the DNS by KMM, Gilbert & Kleiser adopt the spectral approach. Within the near-wall region shown in these figures, the spectra in the streamwise (figure 7d) and circumferential (figure 7e) directions indicate a close similarity between pipe and channel flow.

4.3. *Turbulence flow intensities*

The root-mean-square (r.m.s.) values of the fluctuating velocities, normalized by the friction velocity, are shown in figure 8(a) and compared to the experimental data. From the LDA and HWA measurements only the streamwise velocity fluctuations are obtained; the PIV measurements also provide information on the normal-to-the-wall velocity fluctuations. The available experimental data are in excellent agreement with the DNS results, especially the LDA data. Despite the fact that PIV is better suited to study instantaneous flow structures than to generate flow statistics (see Westerweel *et al.* 1993 and Eggels *et al.* 1993), the PIV results agree well with the numerical and other experimental results. Close to the wall ($r/D > 0.4$) the PIV data are obscured by noise at small scales (see also §4.2) and hence larger r.m.s. velocities are obtained. Furthermore, the PIV measurements yield a larger streamwise r.m.s. velocity at $r/D \sim 0.1$, which should be regarded as a statistical error. The way in which the PIV velocity data are acquired differs from the (one-point) LDA and HWA measurements. In addition to time averaging, line averaging in the homogeneous streamwise direction is also applied (as in DNS). The observed smooth variations of the PIV profiles may appear as a result of the applied data acquisition (for details, we refer to Westerweel 1993). These variations are even more clearly observed in the profile of the Reynolds shear stress shown later on.

In figure 8(b), the present DNS results are compared to those obtained by KMM. The streamwise r.m.s. velocity in the channel flow appears to be slightly lower than in the pipe flow but remains within the scatter of the measurements (see also figure 8a). This smaller r.m.s. velocity is illustrated by the value of maximum r.m.s. velocity equal to 2.73 at $y^+ = 14.1$ in the pipe flow whereas we obtain 2.63 at $y^+ = 14.6$ from KMM's channel flow data. More details on extreme values of second- and higher-order moments of the fluctuating velocities are listed in table 2. The spanwise r.m.s. velocity appears to be little larger at $0.25 < r/D < 0.45$ in the channel than in the pipe. In general, the differences between pipe and channel flow are small indicating that the r.m.s. velocities are much less affected by the different flow geometry than the mean velocity and mean flow properties.

In figure 9 the residual streamwise r.m.s. velocities normalized by u_τ, and calculated in a similar way as the residual mean velocities shown in figure 3 are presented. The LDA and HWA measurements show small residuals ($|\Delta u^+_{z,rms}| < 0.1$) for r/D up to 0.4. Close to the wall the HWA residuals become mainly negative. The smooth variation of the PIV profile is more clearly observed now. The residual r.m.s. velocities are small

FIGURE 6. Two-point correlation coefficients of the three fluctuating velocity components computed from the DNS(E) data as functions of the streamwise separation distance z/D: (a) $r/D = 0.008$, $y^+ = 177.2$; (b) $r/D = 0.247$, $y^+ = 90.9$; (c) $r/D = 0.451$, $y^+ = 17.8$; (d) $r/D = 0.487$, $y^+ = 4.7$.
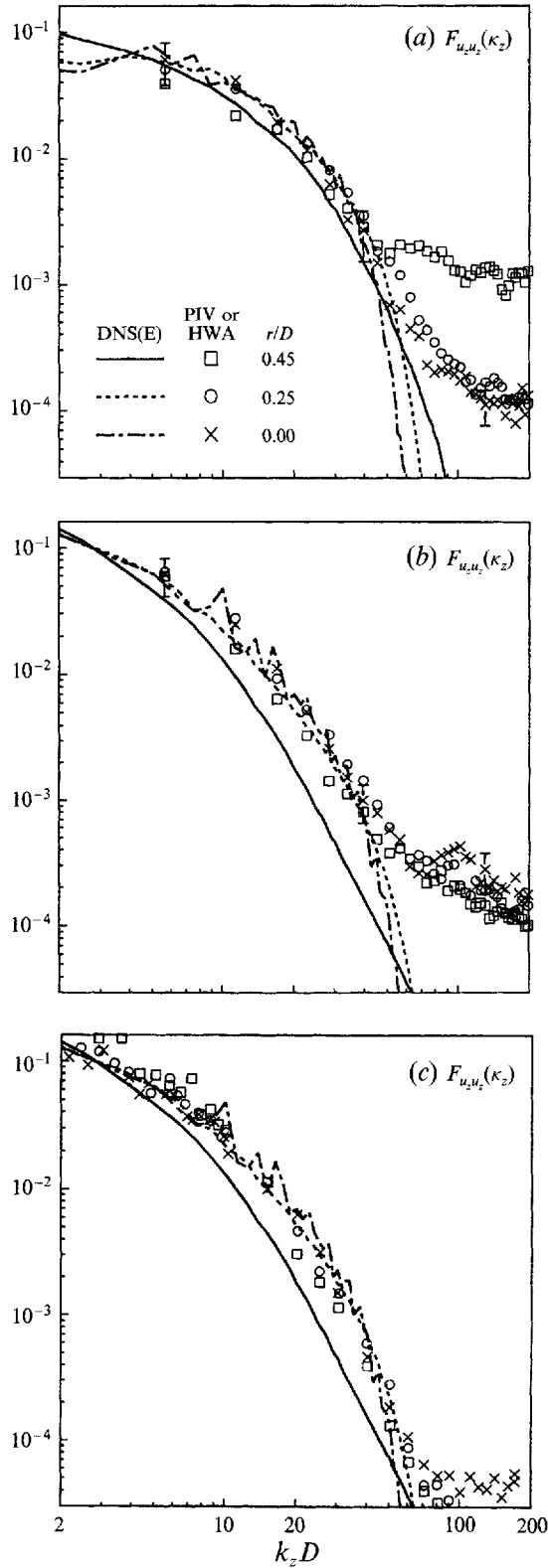
FIGURE 7(*a–c*). For caption see facing page.

$$(d)$$

$$(e)$$
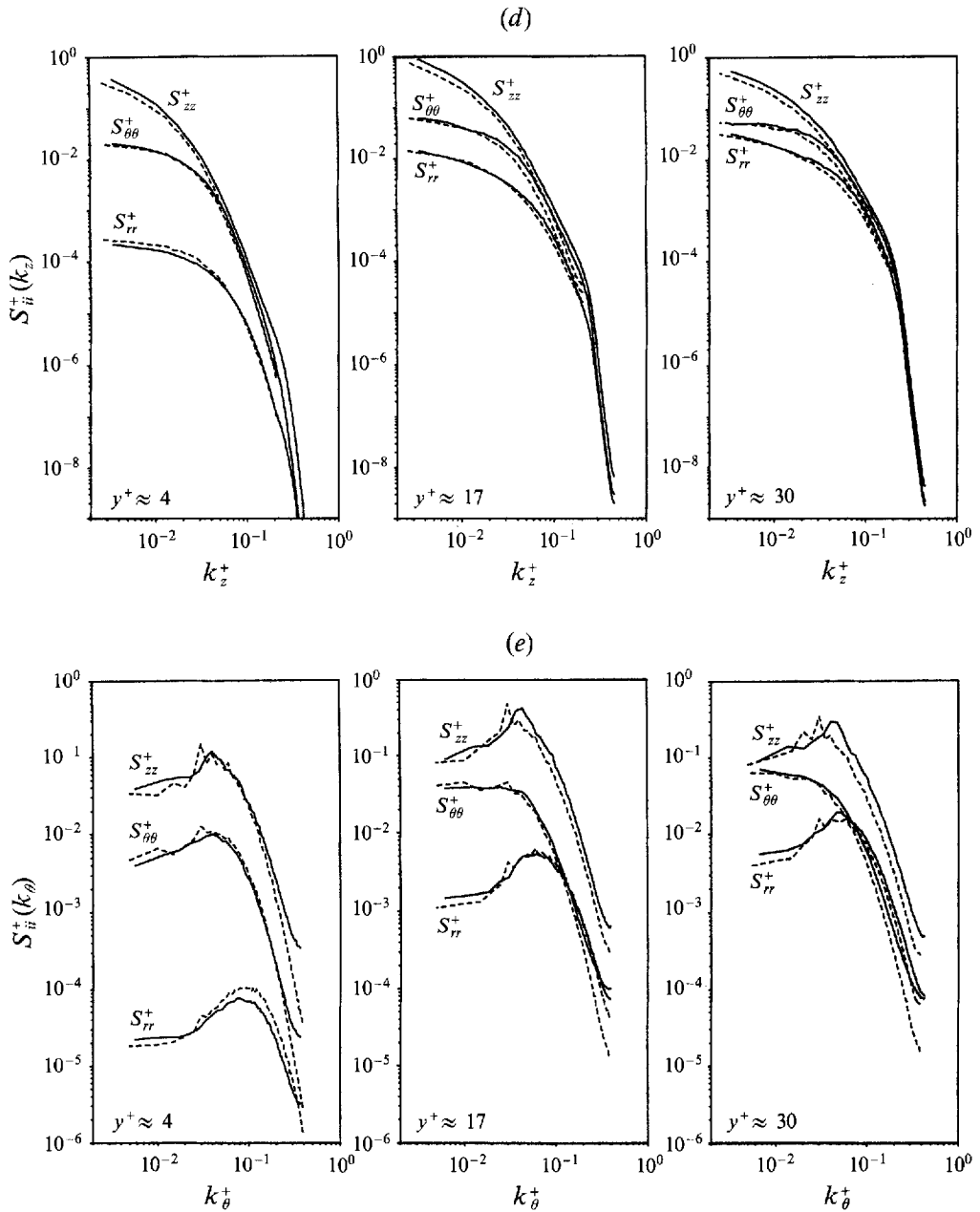
FIGURE 7. One-dimensional wavenumber spectra of the fluctuating velocities: (*a*) and (*b*) comparison between the spectra obtained from DNS(E) and PIV for the radial and axial velocity component; (*c*) comparison between the spectra obtained from DNS(E) and HWA for the axial velocity component; (*d*) and (*e*) comparison between the pipe flow spectra from DNS(U) (solid lines) and the channel flow spectra from Gilbert & Kleiser (1991) (dashed lines) as functions of the streamwise and circumferential wavenumbers for all three velocity components.

and the numerical and experimental results agree to within the 95 % reliability intervals computed for the experimental data. The deviations between DNS(E) and DNS(U) are also small, especially near the wall.

In figure 10(*a*, *b*) the r.m.s. velocities are normalized by the local mean velocity and

	DNS(E)		DNS(U)		DNS(KMM)	
	Value	y^+	Value	y^+	Value	y^+
$u_{r,rms}$	0.832	60.0	0.851	58.1	0.836	55.9
$u_{\theta,rms}$	1.025	44.1	1.031	45.9	1.085	38.1
$u_{z,rms}$	2.731	14.1	2.721	14.1	2.628	14.6
$\overline{u_r' u_z'}$	0.710	32.8	0.729	32.8	0.708	32.8
$S(u_r)$	-0.62	6.6	-0.62	8.4	-0.24	13.3
$S(u_z)$	1.16	0.94	1.07	0.94	0.94	1.02
$F(u_r)$	18.9	1.88	17.3	1.88	$O(22)$	0
$F(u_\theta)$	8.4	0.94	7.9	0.94	$O(7)$	0
$F(u_z)$	2.16	14.1	2.17	14.1	2.15	11.0
$F(u_z)$	5.6	0.94	5.1	0.94	4.1	0

TABLE 2. Several extreme values with the corresponding radial locations of second- and higher-order statistics of the fluctuating velocities. The extreme values of the skewness (S) and flatness (F) factors near the pipe wall are reported at the first location near the wall and have not been extrapolated to the wall where $y^+ = 0$.

plotted only in the near-wall region. The numerical and experimental results show an excellent agreement. The deviations between pipe and channel flow are negligibly small for the streamwise r.m.s. velocity, as shown in figure 10(b). As mentioned before in §2.2, Rai & Moin (1989) repeated the DNS of KMM using finite difference schemes instead of the spectral method. For the central difference scheme, they ended up with a streamwise r.m.s. velocity normalized on the local mean velocity equal to 0.46 at the wall, i.e. clearly different from the 0.36 obtained by KMM and also found here for the pipe flow. They attributed this unsatisfactory result to the central difference scheme. In view of the present results obtained with a similar numerical technique, their unsatisfactory results are most likely caused by the coarse numerical resolution rather than by the application of the central difference scheme itself.

Figure 11 shows the r.m.s. distribution of the pressure fluctuations normalized by ρu_τ^2 along the radial direction. A minimum value at the centreline equal to 0.89 is found whereas KMM reported a minimum value equal to 0.77. A maximum value of 1.83 is obtained in the pipe flow simulations at $y^+ \approx 30$. Close to the wall the root-mean-square value of the pressure fluctuations approaches 1.58 which is in fair agreement with the results of KMM who reported 1.75 at $y^+ \approx 30$ and 1.5 at the wall. Apparently, the pressure fluctuations are rather insensitive to wall curvature as far as the near-wall region is considered. Near the centreline, the pressure fluctuations in the pipe flow are approximately 16% larger than those observed in the plane channel flow. When comparing the r.m.s. values of the pressure fluctuations at the wall with experiments, it appears that the simulations provide rather low values. Schewe (1983), and more recently Löfdahl *et al.* (1993), report P_{rms}/q_∞ of order 0.01 with q_∞ the dynamic pressure of the free stream. Re-scaling with ρu_τ^2 gives P_{rms} equal to 2.6 which is almost a factor 2 larger than the DNS results. Experiments indicate that the size of the transducer can be of significant importance where the r.m.s. value decreases (up to a factor 2) with increasing transducer size (Schewe, 1983; figure 11). Beside a possible Reynolds-number effect (see KMM, end of §4.2), it is not unlikely that the low r.m.s. values obtained from DNS are caused by too coarse a spatial resolution in the streamwise and circumferential directions.
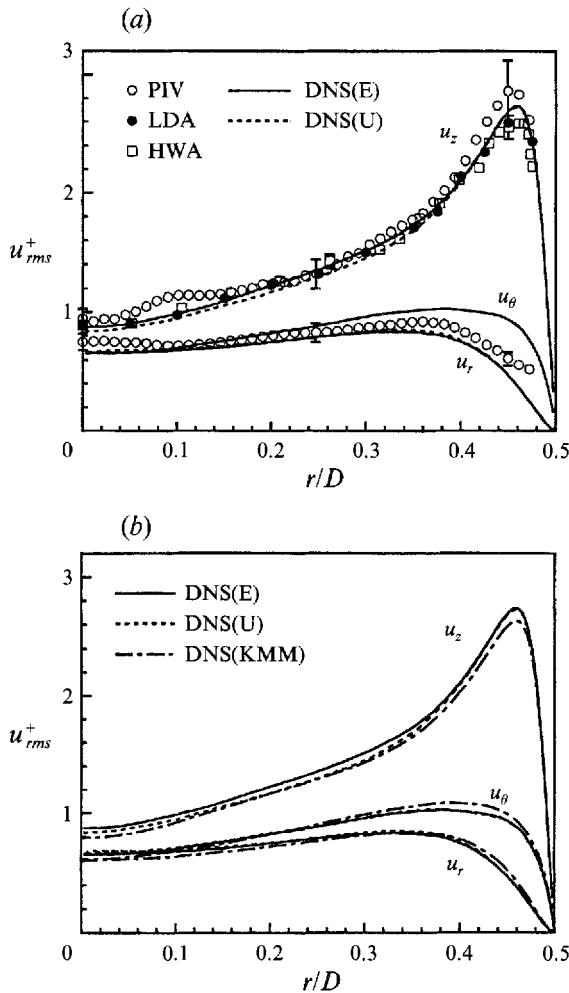
FIGURE 8. Root-mean-square (r.m.s.) velocities normalized by the wall friction velocity u_τ as function of the distance from the centreline: (a) the present numerical and experimental data, (b) a comparison of the present DNS data with the DNS data obtained by KMM for their DNS of turbulent channel flow. The error bars shown for the measurements indicate the 95% reliability intervals computed from the experimental data.

4.4. *Reynolds shear stress*

The Reynolds shear stress and total shear stress are shown in figure 12(a). Since the pipe flow is fully developed and in a statistically steady state, the total shear stress must be linear, which is indeed the case. This linear total shear stress distribution is independent of whether pipe or channel flow is considered because in both cases the normal-to-the-wall gradient of the total shear stress must balance the imposed (fixed) pressure gradient. In the core region of the flow, the viscous shear stresses are small and hence the Reynolds shear stresses in the pipe and channel are similar. Towards the wall, the viscous shear stress becomes important. Deviations in the mean velocity gradient in pipe and channel flow and hence in the viscous shear stress, should induce different Reynolds shear stresses. From figure 12(b) it becomes clear that the Reynolds shear stresses in pipe and channel differ slightly, but that the observed differences are small. As mentioned above, the smooth variations in the PIV shear stress profile may result

(*a*)
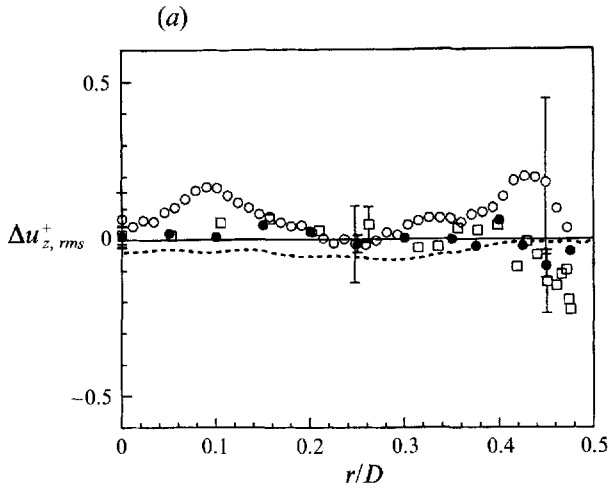
FIGURE 9. Residual axial r.m.s. velocity normalized by the wall friction velocity u_τ as function of the distance from the centreline. The residuals are computed with respect to the DNS(E) data. Symbols as in figure 8.

from the data acquisition procedure used, in combination with a rather limited sample size.

4.5. *Higher-order statistics*

The skewness and flatness factors, S and F respectively, are shown in figures 13(*a–c*) and 14(*a–c*). Here, the differences between pipe and channel flow appear to be somewhat larger than before. The skewness factor of the normal-to-the-wall velocity fluctuations (figure 13*a*) in the channel flow simulation by KMM becomes zero twice at $y^+ \approx 6$ and $y^+ \approx 30$. In contrast, the pipe flow simulations only show one crossover at $y^+ \approx 45$. Near the wall, the skewness factor in the pipe is smaller than in the channel (minimum value approximately -0.6 *vs.* -0.2 in the channel). From its definition, it follows that the skewness factor is related to a normal-to-the-wall energy flux by radial velocity fluctuations. In the pipe flow, this energy flux is negative ($S < 0$) for all $y^+ < 45$ which means that energy is transported towards the pipe wall. In the channel flow, the energy flux changes sign at $y^+ = 6$ and hence energy is transported away from the wall. The latter energy transport requires an energy source or energy supply by other processes near the channel wall. We will return to this point in §5 where the energy budgets are presented.

One could attribute the observed deviations to a different flow geometry, but some care is required. Andersson & Kristoffersen (1992), from their DNS of turbulent channel flow, found behaviour of the skewness factor similar to that found in the present study with only one crossover at $y^+ \approx 40$ but with a larger negative minimum close to -1.7. The agreement of their numerical results with the experiments is not good in the near-wall region (the experimental data used for comparison in their paper closely resemble the results obtained by KMM shown in figure 13*a*). The agreement between the present DNS and PIV results is also not very good, but still reasonable taking into account that the PIV data are obscured by noise close to the wall and hence provide a smaller skewness factor. Detailed experimental investigations focused on the near-wall region should be carried out in the future to clarify the discrepancies observed for the skewness factor. Further numerical investigations should consider the possible influence of streamwise and circumferential gridspacing near the wall before
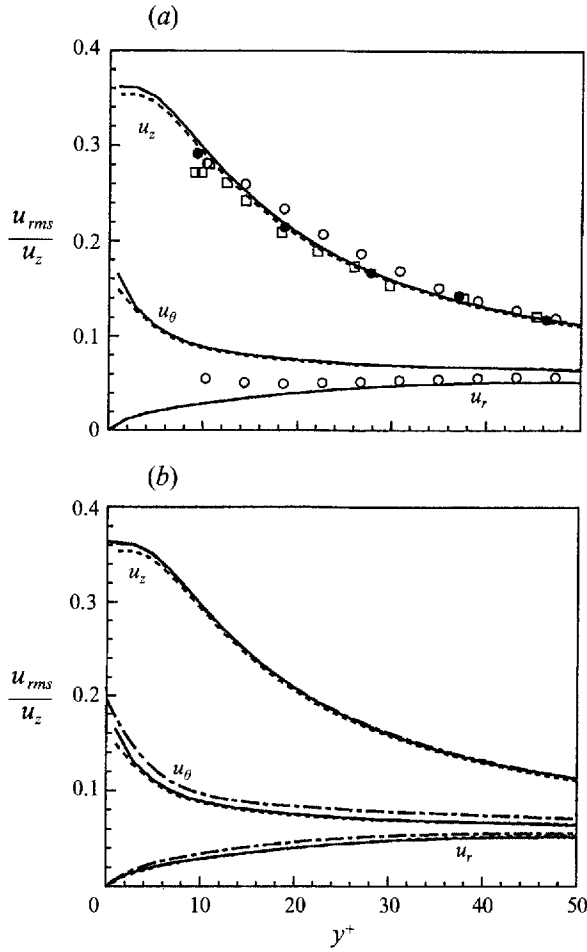
FIGURE 10. Root-mean-square velocities normalized by the local mean velocity in the near-wall region: (*a*) the present numerical and experimental results, (*b*) the present numerical results compared to the channel flow data of KMM. Symbols as in figure 8.
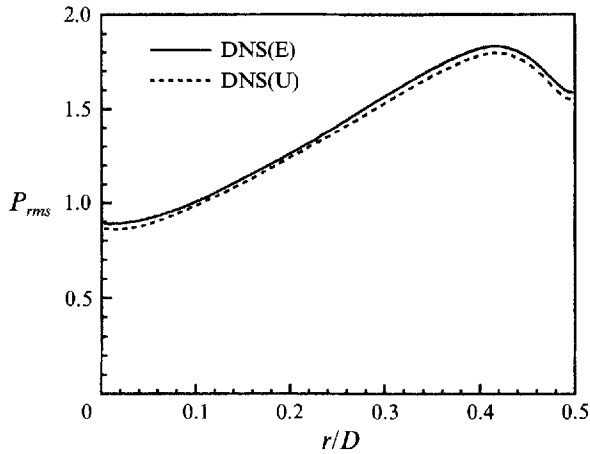
FIGURE 11. Normalized r.m.s. of the pressure fluctuations as a function of the distance from the centreline.
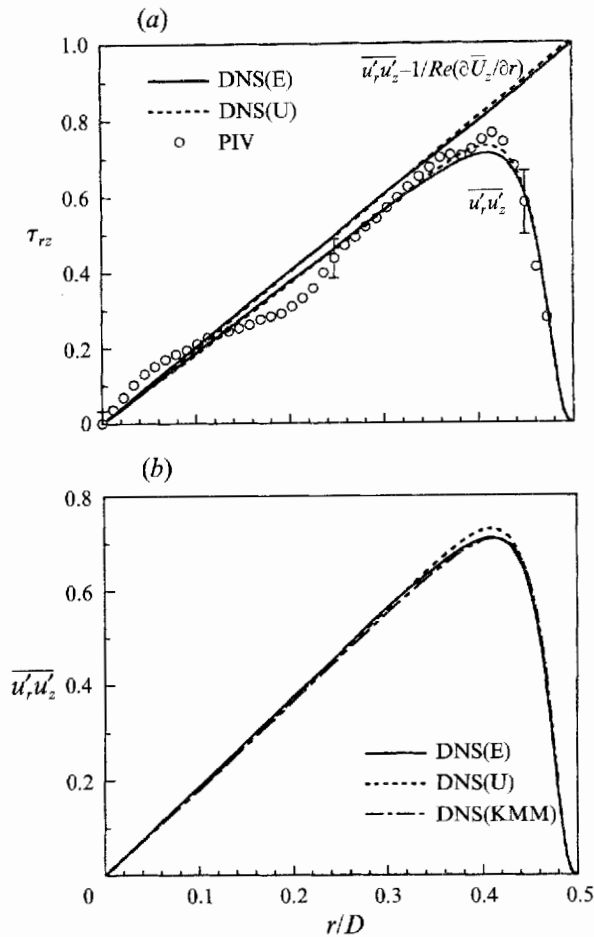
FIGURE 12. Reynolds shear stress and total shear stress distributions, normalized by the shear stress at the wall, as function of r/D: (a) the present numerical and experimental results, (b) a comparison of the Reynolds shear stress in pipe and channel (for plotting purposes, the sign of the shear stress in the channel flow has been inverted).

the observed deviations between pipe and channel flow DNS can be attributed to the different flow geometry.

On the other hand, the skewness factor of the streamwise velocity fluctuations only shows minor deviations between the present and the KMM results (figure 13b). Here, the tendency observed in pipe and channel flow is similar, with a positive skewness near the wall ($y^+ < 10$) and a negative skewness factor approaching -0.5 for $y^+ > 30$; the crossover in the channel flow occurs closer to the wall ($y^+ \approx 10$) than the pipe flow ($y^+ \approx 13$). The numerical and experimental results agree reasonably well except for the PIV measurements at $y^+ > 80$. Because of symmetry, the skewness factor of u'_θ should equal zero. From figure 13(c) it follows that the sample size used here is only marginal since the skewness factor shows some small oscillations and does not equal zero for all y^+.

In contrast to the skewness factor, the flatness factor of u'_r shows the same tendency in channel and pipe flow (figure 14a). The strong increase of the flatness factor up to 20 near the wall is also found in the pipe flow. Andersson & Kristoffersen (1992) even obtained a flatness factor close to 35 at the wall. The corresponding experimental data
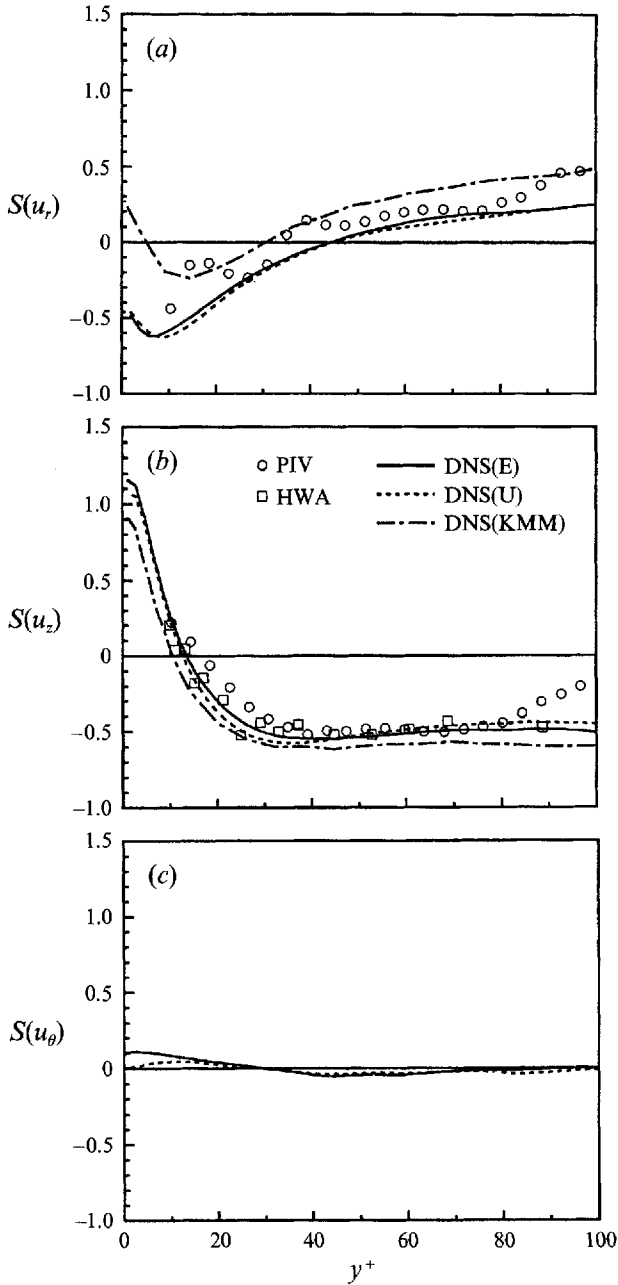
FIGURE 13. Skewness factors of the velocity fluctuations in the near-wall region: (*a*) the normal-to-the-wall velocity component, (*b*) the streamwise velocity component, and (*c*) the circumferential velocity component.

(see KMM and Andersson & Kristoffersen 1992) are questionable, showing a decreasing flatness factor as the wall is approached. This discrepancy between numerical and experimental results regarding the near-wall higher-order moments of the normal-to-the-wall velocity fluctuations, is discussed in detail by KMM. For $y^+ > 30$, the flatness factor is only a little larger than the corresponding value for a Gaussian distribution for which F equals 3.
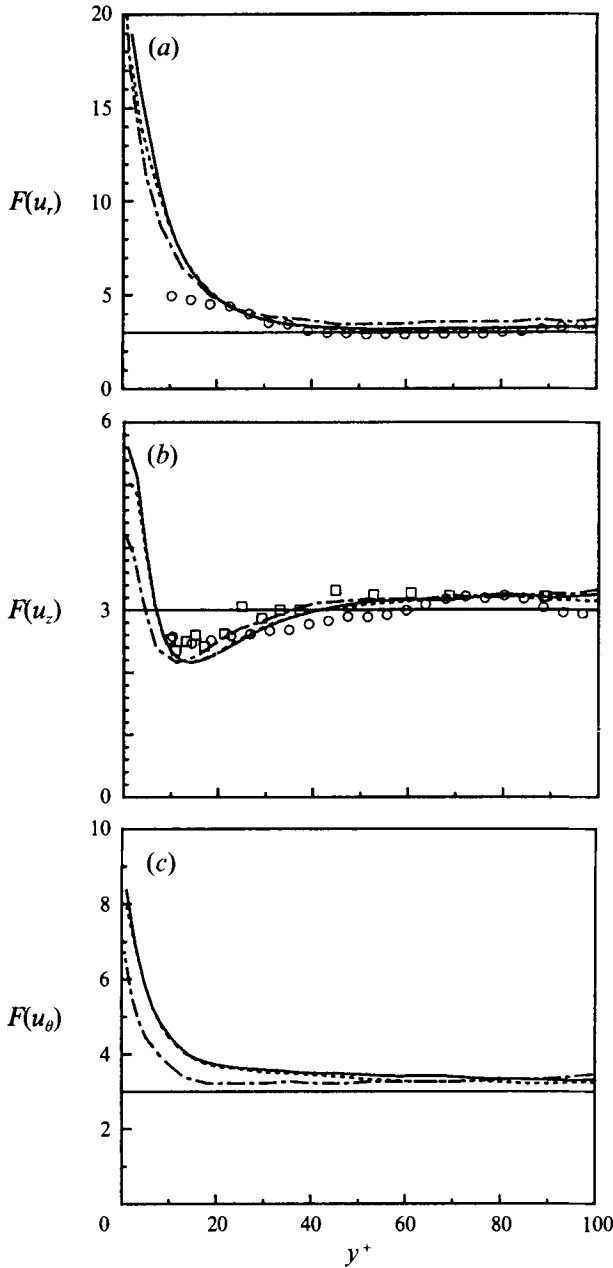
FIGURE 14. As figure 13 but for the flatness factors.

In figure 14(b), the flatness factor for u_z' shows larger deviations between pipe and channel. The two crossovers and the location of the minimum value all occur at larger y^+ in the pipe than in the channel. A similar tendency is observed in the comparison of numerical and experimental channel flow results by KMM (figure 20a of their paper). Here the crossovers in the measurements also occur at larger y^+ than in the simulation. The present DNS data obviously agree well with the experimental data obtained from channel flow. The local minimum flatness factors in pipe and channel flow both equal approximately 2.16 (see also table 2). Near the wall ($y^+ < 10$), the

intermittency of the streamwise velocity fluctuations is larger in the pipe flow as shown by the larger flatness factor (5.6 and 5.1 in DNS(E) and DNS(U) respectively compared to 4.1 in the channel flow). A similar behaviour is found for the flatness factor of the circumferential velocity fluctuations (figure 14c) which is also larger in the pipe than in the channel for $y^+ < 50$. This result is likely to be related to the altered 'splatting' effect in the pipe because of transverse curvature, as explained in §5.

The overall agreement between numerical and experimental third- and fourth-order statistics is reasonable. It should, however, be mentioned that these higher-order statistics are more difficult to obtain with high reliability than for example the second-order statistics because of the large sample size required. In particular, in the PIV measurements the sample size is rather small and hence the higher-order statistics cannot be estimated very accurately. Nevertheless, the PIV results show a reasonable agreement with the DNS and HWA data.

5. Energy balances of the Reynolds stress components

One main advantage of the DNS is the possibility to compute the various terms in the balance equations for the Reynolds-stress components explicitly. In order to obtain these transport equations in cylindrical coordinates we start from the balance equations in general tensor notation, which are obtained from the corresponding formulation of the Navier–Stokes equations, see Moser & Moin (1984) and Bradshaw (1973). The present flow is homogeneous in the axial and circumferential directions. U_z is the only non-zero mean velocity and all derivatives of mean quantities in the circumferential and axial directions vanish. With these simplifications, the budgets for the remaining elements of the Reynolds-stress tensor and the turbulent kinetic energy $k = \frac{1}{2}(\overline{u_r'^2} + \overline{u_\theta'^2} + \overline{u_z'^2})$ are as follows:

$\overline{u_z'^2}$-budget

$$0 = \underbrace{-2\overline{u_r' u_z'}\frac{dU_z}{dr}}_{PR} + \underbrace{2\overline{p'\frac{\partial u_z'}{\partial z}}}_{PS} - \underbrace{\frac{2}{Re}\left[\overline{\left(\frac{\partial u_z'}{\partial r}\right)^2} + \frac{1}{r^2}\overline{\left(\frac{\partial u_z'}{\partial \theta}\right)^2} + \overline{\left(\frac{\partial u_z'}{\partial z}\right)^2}\right]}_{DS}$$

$$\underbrace{-\frac{1}{r}\frac{\partial(r\overline{u_r' u_z'^2})}{\partial r}}_{TD} + \underbrace{\frac{1}{Re}\left[\frac{1}{r}\frac{\partial}{\partial r}\left(r\frac{\partial \overline{u_z'^2}}{\partial r}\right)\right]}_{VD}; \quad (6)$$

$\overline{u_\theta'^2}$-budget

$$0 = \underbrace{\frac{2}{r}\overline{p'\left(\frac{\partial u_\theta'}{\partial \theta} + u_r'\right)}}_{PS} - \underbrace{\frac{2}{Re}\left[\overline{\left(\frac{\partial u_\theta'}{\partial r}\right)^2} + \frac{1}{r^2}\overline{\left(\frac{\partial u_\theta'}{\partial \theta} + u_r'\right)^2} + \overline{\left(\frac{\partial u_\theta'}{\partial z}\right)^2}\right]}_{DS}$$

$$\underbrace{-\frac{1}{r}\frac{\partial(r\overline{u_r' u_\theta'^2})}{\partial r} - \frac{2}{r}\overline{u_r' u_\theta'^2}}_{TD} \underbrace{- \frac{2}{r}\overline{u_r' p'}}_{PD} + \underbrace{\frac{1}{Re}\left[\frac{1}{r}\frac{\partial}{\partial r}\left(r\frac{\partial \overline{u_\theta'^2}}{\partial r}\right) - \frac{2}{r^2}(\overline{u_\theta'^2} - \overline{u_r'^2})\right]}_{VD}; \quad (7)$$

$\overline{u_r'^2}$-budget

$$0 = \underbrace{2\overline{p'\frac{\partial u_r'}{\partial r}}}_{PS} - \underbrace{\frac{2}{Re}\left[\overline{\left(\frac{\partial u_r'}{\partial r}\right)^2} + \frac{1}{r^2}\overline{\left(\frac{\partial u_r'}{\partial \theta} - u_\theta'\right)^2} + \overline{\left(\frac{\partial u_r'}{\partial z}\right)^2}\right]}_{DS}$$
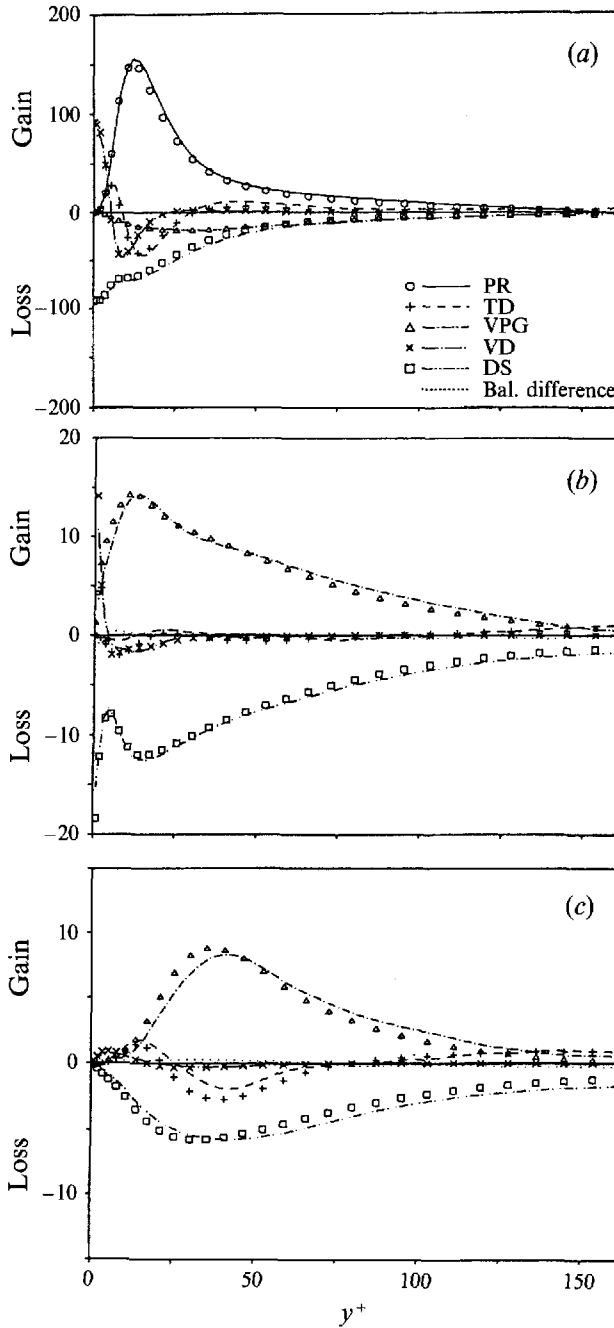
FIGURE 15. Terms in the Reynolds-stress budgets of the fluctuating velocity components in wall coordinates: (*a*) the streamwise velocity component, (*b*) the circumferential velocity component and (*c*) the normal-to-the-wall velocity component. The symbols denote the corresponding terms for the channel flow data reported by Mansour *et al.* (1988). The pipe flow budgets are computed from the DNS(U) data.

$$-\frac{1}{r}\frac{\partial(r\overline{u_r'u_r'^2})}{\partial r}+\frac{2}{r}\overline{u_r'u_\theta'^2}-2\frac{\overline{(\partial u_r'p')}}{\partial r}+\frac{1}{Re}\left[\frac{1}{r}\frac{\partial}{\partial r}\left(r\frac{\partial\overline{u_r'^2}}{\partial r}\right)+\frac{2}{r^2}(\overline{u_\theta'^2}-\overline{u_r'^2})\right]; \quad (8)$$

$$\underbrace{\phantom{-\frac{1}{r}\frac{\partial(r\overline{u_r'u_r'^2})}{\partial r}+\frac{2}{r}\overline{u_r'u_\theta'^2}}}_{\text{TD}}\quad\underbrace{\phantom{-2\frac{\overline{(\partial u_r'p')}}{\partial r}}}_{\text{PD}}\quad\underbrace{\phantom{\frac{1}{Re}\left[\frac{1}{r}\frac{\partial}{\partial r}\left(r\frac{\partial\overline{u_r'^2}}{\partial r}\right)+\frac{2}{r^2}(\overline{u_\theta'^2}-\overline{u_r'^2})\right]}}_{\text{VD}}$$

$\overline{u_r'u_z'}$-budget

$$0=\underbrace{-\overline{u_r'u_r'}\frac{\mathrm{d}U_z}{\mathrm{d}r}}_{\text{PR}}+\underbrace{\overline{p'\left(\frac{\partial u_z'}{\partial r}+\frac{\partial u_r'}{\partial z}\right)}}_{\text{PS}}-\underbrace{\frac{2}{Re}\left[\overline{\frac{\partial u_r'}{\partial r}\frac{\partial u_z'}{\partial r}}+\frac{1}{r^2}\overline{\left(\frac{\partial u_r'}{\partial\theta}-u_\theta'\right)\frac{\partial u_z'}{\partial\theta}}+\overline{\frac{\partial u_r'}{\partial z}\frac{\partial u_z'}{\partial z}}\right]}_{\text{DS}}$$

$$-\frac{1}{r}\frac{\partial(r\overline{u_r'^2u_z'})}{\partial r}+\frac{1}{r}\overline{u_\theta'^2u_z'}-\frac{\partial(\overline{u_z'p'})}{\partial r}+\frac{1}{Re}\left[\frac{1}{r}\frac{\partial}{\partial r}\left(r\frac{\partial(\overline{u_r'u_z'})}{\partial r}\right)-\frac{1}{r^2}\overline{u_r'u_z'}\right]; \quad (9)$$

$$\underbrace{\phantom{-\frac{1}{r}\frac{\partial(r\overline{u_r'^2u_z'})}{\partial r}+\frac{1}{r}\overline{u_\theta'^2u_z'}}}_{\text{TD}}\quad\underbrace{\phantom{-\frac{\partial(\overline{u_z'p'})}{\partial r}}}_{\text{PD}}\quad\underbrace{\phantom{\frac{1}{Re}\left[\frac{1}{r}\frac{\partial}{\partial r}\left(r\frac{\partial(\overline{u_r'u_z'})}{\partial r}\right)-\frac{1}{r^2}\overline{u_r'u_z'}\right]}}_{\text{VD}}$$

k-budget

$$0=\underbrace{-\overline{u_r'u_z'}\frac{\mathrm{d}U_z}{\mathrm{d}r}}_{\text{PR}}-\underbrace{\epsilon}_{\text{DS}}-\underbrace{\frac{1}{r}\frac{\mathrm{d}}{\mathrm{d}r}(r\overline{u_r'k})}_{\text{TD}}-\underbrace{\frac{1}{r}\frac{\mathrm{d}}{\mathrm{d}r}(r\overline{u_r'p'})}_{\text{PD}}+\underbrace{\frac{1}{Re}\left[\frac{1}{r}\frac{\mathrm{d}}{\mathrm{d}r}\left(r\frac{\mathrm{d}k}{\mathrm{d}r}\right)\right]}_{\text{VD}}. \quad (10)$$

Terms on the right-hand sides of (6)–(10) have the following meaning: production PR, pressure strain PS, dissipation DS, turbulent diffusion TD, pressure diffusion PD and viscous diffusion VD. The two pressure terms can be combined to form the velocity–pressure gradient term VPG. Other ways of splitting the VPG term are discussed by Mansour, Kim & Moin (1988).

Figure 15(*a–c*) shows the budgets computed from the DNS(U) data for the turbulence intensities, and figures 18 and 19 those for the Reynolds shear stress and the turbulent kinetic energy in local wall coordinates. The range of the non-dimensionalized wall distance is $0\leqslant y^+\leqslant 162$. In terms of radial distance, this corresponds to the range $0.5\geqslant r/D\geqslant 0.05$. In the region close to the pipe axis ($162\leqslant y^+\leqslant 180$) it is difficult to calculate all terms in the budgets correctly because of the singularity at the pipe centreline (terms involving $1/r$ become extremely dominant near the centreline). All terms plotted are scaled by u_τ^3/D. In addition, the balance difference is drawn. The results are compared to the DNS channel flow data of KMM reported by Mansour *et al.* (1988).

The plots of the three turbulence intensities show the typical characteristics of these components. The $\overline{u_z'^2}$-budget is largely dominated by production and dissipation away from the wall. While the turbulent diffusion term becomes positive at about $y^+=10$, the viscous diffusion changes sign at $y^+=5$. At the wall the dissipation rate balances the viscous diffusion rate. The pressure–strain term which equals the velocity–pressure gradient term is negative over the whole pipe radius. This term takes away energy from the axial component and redistributes it among the other two components. Obviously, in the near-wall region transverse curvature effects are small in the five balance terms of figure 15(*a*). However, the PS_{zz} term (plotted in figure 16) is altered slightly close to the wall compared to the channel flow, which seems to result from an alteration of the splatting effect due to transverse curvature (see below).

The $\overline{u_\theta'^2}$-balance reveals an equilibrium between dissipation and the velocity–pressure gradient term away from the wall. As in channel flow, the turbulent transport term remains small with respect to the other terms. Very close to the wall viscous diffusion becomes the dominant source term. At the wall itself, it balances the dissipation rate. The VPG term is slightly affected by transverse curvature in the vicinity of the wall.
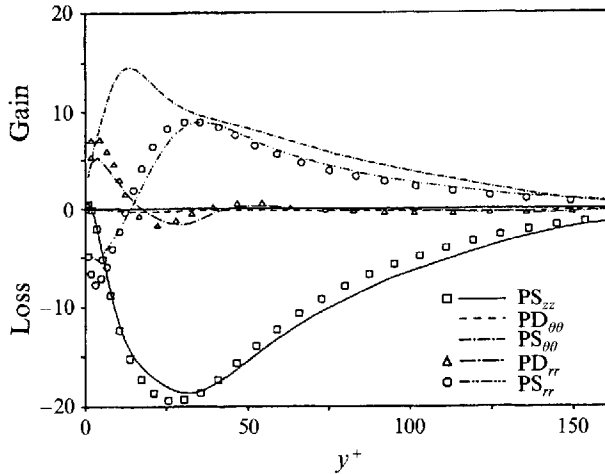
FIGURE 16. Splitting of the velocity–pressure-gradient term (VPG) into the pressure–strain (PS) and the pressure–diffusion (PD) terms. The symbols mark the corresponding terms for the channel flow data reported by Mansour *et al.* (1988).

In the $\overline{u_r'^2}$-budget there is also no production term, thus the dissipation and the velocity–pressure gradient term are again the dominant ones. Viscous diffusion has a smaller influence here than for the other two Reynolds-stress components. The PS and PD terms in this budget are directly affected by transverse curvature close to the wall through the splatting effect explained by Mansour *et al.* (1988). This effect is connected with sweep events which carry high-speed fluid to the wall and thus produce a flow pattern similar to that of a jet impinging upon a wall with a net energy transfer to the circumferential and longitudinal components (splatting). Contour lines of a snapshot of the longitudinal velocity fluctuations in figure 17 give an impression of sweep and ejection events. The mushroom-like structures close to the wall drawn as solid lines correspond to high-speed fluid. Now, owing to transverse curvature of the wall the spreading of fluid in the circumferential direction is inhibited. This phenomenon is reflected in the magnitudes of PS_{rr} and PD_{rr} in the immediate wall vicinity. A comparison between pipe and channel flow in figure 16 reveals smaller values of both terms close to the pipe wall. Also, further away from the wall ($y^+ \approx 20$) the PS_{rr} and PD_{rr} terms in the pipe and channel differ. In the budget for $\overline{u_r'^2}$, however, PS_{rr} and PD_{rr} terms do not appear individually but together, which means that their sum (the VPG term) is important. From figure 15(*c*), it appears that, like the two individual contributions, the VPG term differs in pipe and channel flow. Alteration of this gain term induces changes of the TD and DS terms to satisfy the proper balance. As a result, the triple correlations of the radial velocity fluctuations (see figure 13*a*), which are associated with the TD term, show deviations from the channel data.

In figure 16, the velocity–pressure gradient terms are split into pressure–diffusion and pressure–strain terms to confirm the physical interpretation of the latter. No pressure–diffusion term exists in the $\overline{u_z'^2}$-budget; this term is only important in the $\overline{u_r'^2}$-budget close to the wall. As expected, in the fully turbulent region the pressure–strain term redistributes energy from the axial into the circumferential and the radial components. Therefore the sum of all pressure–strain terms vanishes. In the $\overline{u_r'^2}$- and the $\overline{u_\theta'^2}$-budgets the pressure–strain terms are the most important source terms. Only near the wall where $y^+ \leqslant 14$ does the pressure–strain term in the $\overline{u_r'^2}$-budget become negative whereas the pressure–diffusion term becomes positive and of comparable
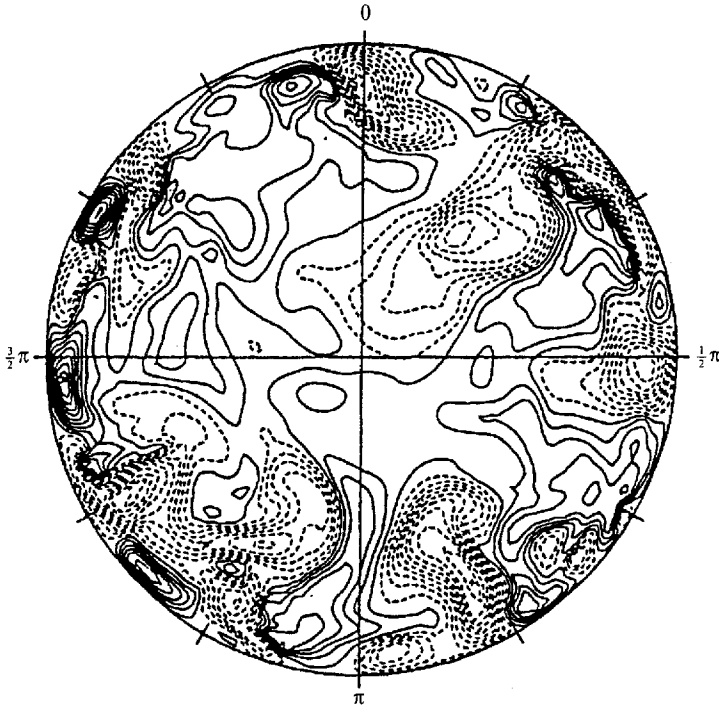
FIGURE 17. Contour lines of the fluctuating axial velocity component in a cylindrical cross-section of the flow. Positive contours are shown as solid lines and negative contours are dashed. The minimum value is -6.211, the maximum is 6.183 and the increment is 0.6523.
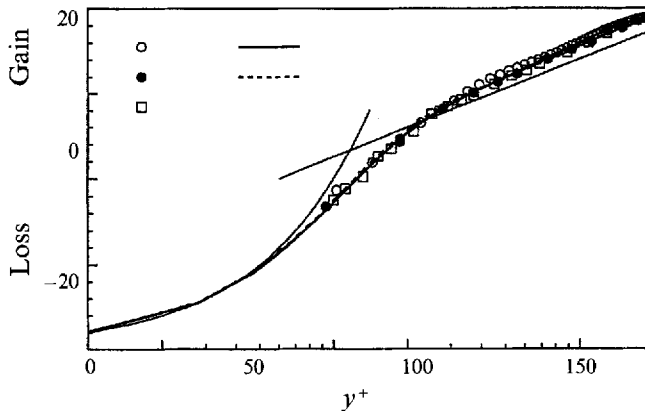
FIGURE 18. Terms in the energy budget of the Reynolds shear stress (for details, see the caption of figure 15).

magnitude to the pressure–strain term (the VPG term is close to zero). In this region the PS_{rr} term is the dominant sink term and redistributes energy from the $\overline{u_r'^2}$-budget into the $\overline{u_\theta'^2}$-budget. This is due to the 'splatting' or 'impingement' effect, explained above.

Figure 18 shows the budget for the Reynolds shear stress. It is dominated by the production and the velocity–pressure gradient term. Away from the wall, VPG
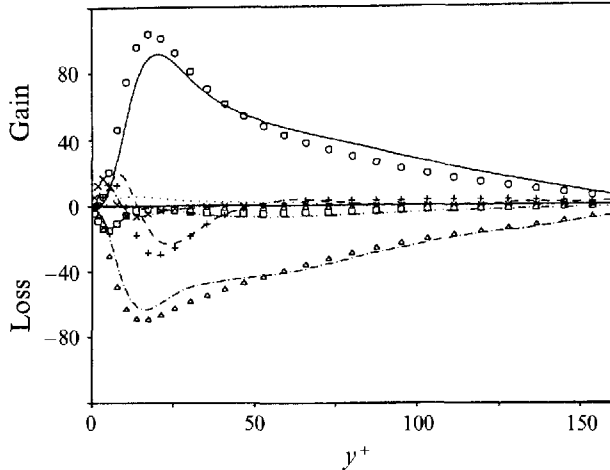
FIGURE 19. Terms in the energy budget of the turbulent kinetic energy
(for details, see the caption of figure 15).

balances PR while the other terms are small. In the wall layer TD becomes important. In between the viscous sublayer and the buffer layer, the VD and DS terms reach extreme absolute values. The sum of both terms, however, is small in the whole flow field, which means that viscosity has practically no influence on this quantity. The observed deviations between the pipe and channel flow budgets are most likely caused by implicit curvature effects via the radial velocity fluctuations. Despite the deviations in the budgets, the Reynolds shear stress in the pipe and channel are in very close agreement (figure 12b).

In figure 19 the results for the three turbulence intensities are summed up in the budget for the turbulent kinetic energy. Comparing the magnitude of the terms of the three components it is obvious that the k-budget is very simular to the $\overline{u_z'^2}$-budget. The pressure–velocity gradient term consists only of the pressure diffusion term and is of minor importance. There are great similarities in the k-budgets of pipe and channel flow. Only the turbulent diffusion term reflects minor effects of transverse curvature in the radial transport of kinetic energy away from the wall.

6. Summary and conclusions

Direct numerical simulations and experiments have been carried out to study fully developed turbulent pipe flow at a Reynolds number of $Re_c \approx 7000$ based on centreline velocity and pipe diameter. The flow statistics obtained from two different numerical codes and three different measurement techniques (hot-wire anemometry (HWA), laser Doppler anemometry (LDA) and particle image velocimetry (PIV)) are compared and a good agreement between direct numerical simulation and experiment is obtained. This good agreement of statistical results demonstrates that the present numerical codes based on the finite volume technique in cylindrical coordinates, provide realistic turbulent flow statistics.

To investigate the differences between fully developed flow in an axisymmetric pipe and a plane channel geometry, the present numerical results are compared with the statistical results of Kim *et al.* (1987) (KMM). To avoid any Reynolds-number effects, the Reynolds number used in our study exactly matches the Reynolds number employed by KMM. Previous studies on the differences between axisymmetric and

plane channel flow only considered the mean velocities and not the statistics on velocity fluctuations. Patel & Head (1969) have already reported observed differences in mean velocity profiles obtained from fully developed turbulent channel and pipe flow measurements. They demonstrated that the flow in a pipe fails to conform to the accepted law of the wall even at Reynolds numbers considerably above 3000, in contrast to channel flows. The results of the present study indeed confirm their observations. Whereas the channel flow data follow the logarithmic velocity distribution up to the channel centreline, the numerical and experimental pipe flow data significantly exceed this logarithmic velocity distribution for $y^+ > 30$. In the centre region of the flow ($y^+ > 50$), the mean velocities in the pipe and channel deviate by up to $1.2u_\tau$. The deviations between experimental and numerical pipe flow results are much smaller ($< 0.4u_\tau$), which confirms the difference between axisymmetric and plane channel flow. The differences in the mean velocity profile are also reflected in several parameters which are related to the mean velocity profile. The ratio U_b/u_τ in the plane geometry is about 6% larger than in the axisymmetric geometry, whereas the ratio U_c/U_b is about 12% smaller. These changes are caused by the additional friction at the 'side'-walls of the pipe which is absent in the plane channel. In a square duct flow, where there is also additional friction at the sidewalls, the ratios mentioned above are almost the same as for the axisymmetric pipe geometry (deviations are approximately 0.5% and 1.5% respectively).

The statistics on fluctuating velocities appear to be less affected by the cylindrical cross-section of the pipe geometry. The streamwise r.m.s. velocities in the channel are only slightly smaller than in the pipe whereas the spanwise r.m.s. velocities are somewhat larger for r/D between 0.25 and 0.45. Typical deviations between pipe and channel flow are of the order of $0.1u_\tau$. The deviations between experimental and numerical r.m.s. velocities in the pipe are also of the order of $0.1u_\tau$. This illustrates that the observed differences in pipe and channel flow for the turbulence intensities are largely insignificant. Larger deviations are observed for the higher-order statistics of the fluctuating velocities. In particular, the skewness factor of the normal-to-the-wall velocity fluctuations differs from the results obtained in the channel. A physical explanation for the observed differences must start from the impingement mechanism at the wall which is altered by transverse curvature effects. All other higher-order statistics obtained from the present pipe flow simulations show a quite fair agreement with the results from the plane channel flow simulation.

We also computed the energy budgets of the Reynolds-stress components. A comparison of these budgets with the corresponding results from the plane channel flow shows an excellent agreement, except for the terms involving the normal-to-the-wall velocity fluctuations. Here, the tendency in the budgets is similar, but the radial locations of local extremes and crossovers show small discrepancies. These discrepancies must be associated with the altered impingement mechanism at the wall. In particular the pressure–strain and pressure–diffusion terms in the $\overline{u_r'^2}$-budget show magnitudes decreased by up to 35% in the near-wall region ($y^+ < 10$) compared to the plane channel flow results.

REFERENCES

ANDERSSON, H. I. & KRISTOFFERSEN, R. 1992 Statistics of numerically generated turbulence. *Acta Applicandae Mathematicae* **26**, 293–314.

ANTONIA, R. A., TEITEL, M., KIM, J. & BROWNE, L. W. B. 1992 Low-Reynolds-number effects in a fully developed turbulent channel flow. *J. Fluid Mech.* **236**, 579–605.

BRADSHAW, P. 1973 The effects of streamline curvature on turbulent flow. *AGARDograph* 169.

ECKELMANN, H. 1974 The structure of the viscous sublayer and the adjacent wall region in a turbulent channel flow. *J. Fluid Mech.* **65**, 439–459.

EGGELS, J. G. M. 1994 Direct and large eddy simulation of turbulent flow in a cylindrical pipe geometry. PhD thesis, Delft University of Technology, the Netherlands.

EGGELS, J. G. M., WESTERWEEL, J., NIEUWSTADT, F. T. M. & ADRIAN, R. J. 1993 Comparison of vortical flow structures in DNS and PIV studies of turbulent pipe flow. In *Near-Wall Turbulent Flows* (ed. R. M. C. So *et al.*), pp. 413–422. Elsevier.

GAVRILAKIS, S. 1992 Numerical simulation of low-Reynolds-number turbulent flow through a straight square duct. *J. Fluid Mech.* **244**, 101–129.

GILBERT, N. & KLEISER, L. 1991 Turbulence model testing with the aid of direct numerical simulation results. *Proc. 8th Symp. on Turbulent Shear Flows, Sept. 9–11, Munich, Germany.*

GRÖTZBACH, G. 1983 Spatial resolution requirements for direct numerical simulation of the Rayleigh–Bénard convection. *J. Comput. Phys.* **49**, 241–264.

HUFFMAN, G. D. & BRADSHAW, P. 1972 A note on von Kármán's constant in low Reynolds number turbulent flows. *J. Fluid Mech.* **53**, 45–60.

KIM, J., MOIN, P. & MOSER, R. 1987 Turbulence statistics in fully developed channel flow at low Reynolds number. *J. Fluid Mech.* **177**, 133–166 (referred to herein as KMM).

KREPLIN, H. & ECKELMANN, H. 1979 Behavior of the three fluctuating velocity components in the wall region of a turbulent channel flow. *Phys. Fluids* **22**, 1233–1239.

KRISTOFFERSEN, R. & ANDERSSON, H. I. 1993 Direct simulations of low Reynolds number turbulent flow in a rotating channel. *J. Fluid Mech.* **256**, 163–197.

LANDRETH, C. C. & ADRIAN, R. J. 1990 Measurement and refinement of velocity data using high image density analysis in particle image velocimetry. In *Applications of Laser Anemometry to Fluid Mechanics* (ed. R. J. Adrian *et al.*), pp. 484–497. Springer.

LAUFER, J. 1954 The structure of turbulence in fully developed pipe flow. *NACA Rep.* 1174.

LAWN, C. J. 1971 The determination of the rate of dissipation in turbulent pipe flow. *J. Fluid Mech.* **48**, 477–505.

LEKAKIS, I. C. 1988 Coherent structures in fully developed turbulent pipe flow. Thesis University of Illinois.

LÖFDAHL, L., GLAVMO, M., JOHANSSON, B. & STEMME, G. 1993 A silicon transducer for the determination of wall-pressure fluctuations in turbulent boundary layers. *Appl. Sci. Res.* **51**, 203–207.

LYONS, S. L., HANRATTY, T. J. & MCLAUGHLIN, J. B. 1991 Large-scale computer simulation of fully developed turbulent channel flow with heat transfer. *Intl J. Numer. Meth. Fluids* **13**, 999–1028.

MANSOUR, N. N., KIM, J. & MOIN, P. 1988 Reynolds-stress and dissipation-rate budgets in a turbulent channel flow. *J. Fluid Mech.* **194**, 15–44.

MOSER, R. D. & MOIN, P. 1984 Direct numerical simulation of curved turbulent channel flow. *Rep.* TF-20. Stanford University.

PATEL, V. C. & HEAD, M. R. 1969 Some observations on skin friction and velocity profiles in fully developed pipe and channel flows. *J. Fluid Mech.* **38**, 181–201.

RAI, M. M. & MOIN, P. 1989 Direct simulations of turbulent flow using finite difference schemes. *AIAA Paper* 89-0369 (also in *J. Comput. Phys.* **96**, 15–53, 1991).

SCHEWE, G. 1983 On the structure and resolution of wall-pressure fluctuations associated with turbulent boundary-layer flow. *J. Fluid Mech.* **134**, 311–328.

SCHLICHTING, H. 1979 *Boundary-Layer Theory*, 7th edn., pp. 596–612. McGraw-Hill.

SCHUMANN, U. 1973 Ein Verfahren zur direkten numerischen Simulation turbulenter Strömungen in Platten- und Ringspaltkanälen und über seine Anwendung zur Untersuchung von Turbulenzmodellen. PhD thesis, KFK 1854, TH Karlsruhe, Germany.

SCHUMANN, U. 1975 Linear stability of finite difference equations for three-dimensional flow problems. *J. Comput. Phys.* **18**, 465–470.

SPALART, P. R. 1988 Direct simulation of a turbulent boundary layer up to $Re_\theta = 1410$. *J. Fluid Mech.* **187**, 61–98.

TENNEKES, H. & LUMLEY, J. L. 1972 *A First Course in Turbulence*. MIT Press.

UNGER, F. & FRIEDRICH, R. 1993 Large eddy simulation of fully-developed turbulent pipe flow. In *Flow Simulation of High Performance Computers I* (ed. E. H. Hirschel), NNFM, Vol. 38, pp. 201–216. Vieweg (also in *Proc. 8th Symp. on Turbulent Shear Flows, Sept. 9–11, 1991, Munich, Germany,* pp. 19/3/1–19/3/6).

WEI, T. & WILLMARTH, W. W. 1989 Reynolds-number effects on the structure of a turbulent channel flow. *J. Fluid Mech.* **204**, 57–95.

WEISS, M. H. 1993 Drag reduction with riblets in pipe flow. PhD thesis, University of Calgary, Canada.

WESTERWEEL, J. 1993 Digital particle image velocimetry: theory and application. PhD thesis, Delft University of Technology, the Netherlands.

WESTERWEEL, J., ADRIAN, R. J., EGGELS, J. G. M. & NIEUWSTADT, F. T. M. 1993 Measurements with particle image velocimetry of fully developed turbulent pipe flow at low Reynolds number. In *Laser Applications in Fluid Mechanics* (ed. R. J. Adrian *et al.*) Springer. (also in *Proc. 6th Intl Symp. on Applications of Laser Techniques to Fluid Mechanics, July 20–23, 1992, Lisbon, Portugal* Paper 1.2).

WYGNANSKI, I. J. & CHAMPAGNE, F. H. 1973 On transition in a pipe. Part 1. The origin of puffs and slugs and the flow in a turbulent slug. *J. Fluid Mech.* **59**, 281–335.